


 Cite this: *RSC Adv.*, 2021, **11**, 34963

## Evaluation of histone deacetylase inhibitor substituted zinc and indium phthalocyanines for chemo- and photodynamic therapy†

 Başak Aru,<sup>a</sup> Aysel Günay,<sup>b</sup> Gülderen Yanikkaya Demirel,<sup>\*a</sup> Ayşe Gül Gürek  <sup>\*b</sup> and Devrim Atilla 

In this study, we synthesized and characterized 3-hydroxypyridin-2-thione (3-HPT) bearing zinc (**ZnPc-1** and **ZnPc-2**) and indium (**InPc-1** and **InPc-2**) phthalocyanine (Pc) derivatives, either non-peripherally or peripherally substituted as photosensitizer (PS) agents and evaluated their anti-cancer efficacy on two breast cancer cell lines, MDA-MB-231 and MCF-7 as well as a human endothelial cell line, HUVEC. Our results indicated different localization patterns between **ZnPcs** and **InPcs** in addition to enhanced effects on the mitochondrial network for **InPcs**. Moreover, peripheral or non-peripheral substitution of **HDACi** moieties altered cellular localization between **ZnPc-1** and **ZnPc-2**, leading to increased  $IC_{50}$  values along with decreased anti-cancer activity for non-peripheral substitution. When considering the compounds' differential effects *in vitro*, our data indicates that further research is required to determine the ideal Pcs for anti-cancer PDT treatments since the core metals of the compounds have affected the cellular localization, and positioning of the chemotherapeutic residues may inhibit cellular penetrance.

 Received 14th July 2021  
 Accepted 14th October 2021

DOI: 10.1039/d1ra05404j

[rsc.li/rsc-advances](http://rsc.li/rsc-advances)

### Introduction

Consisting of a photosensitizer (PS), light, and oxygen; photodynamic therapy (PDT) aims to destroy malignant tissue *via* irradiating the PS by a light source at a wavelength matching the compound's absorption maximum.<sup>1,2</sup> Irradiation promotes chemical reactions that are induced by electron or energy transfer; in turn, reactive oxygen and nitrogen species are generated. PDT exerts its anti-cancer effects mainly by a highly reactive state of oxygen, so-called singlet oxygen ( $^1O_2$ ),<sup>3</sup> and targets tumours *via* three distinct mechanisms. Irradiation of the PS promotes accumulation of reactive oxygen species (ROS) that directly kill tumour cells by activating programmed cell death mechanisms.<sup>4,5</sup> PDT can impair tumour associated vascularization and leads to nutrient and oxygen deprivation, moreover, PDT-induced stress signals also enable the immune system to recognise and destroy tumour cells.<sup>6,7</sup> The role of each mechanism depends on the type and dose of the PS administered, incubation duration of the target tissue with the PS, optical dose of irradiation and tumour oxygen levels,<sup>6</sup> and all three mechanisms mentioned above are important for tumour regression<sup>8,9</sup> while the importance of each in tumour

eradication needs further research. Among other PSs such as tetrapyrrolic porphyrins and chlorins, thanks to their high extinction coefficients and longer absorption wavelengths (due to additional benzene rings connected to each pyrrolic subunit which causes more electron delocalization),<sup>10,11</sup> phthalocyanines (Pcs) are regarded as potent second-generation PS compounds in cancer treatment. The efficacy and specificity of the treatment can be further increased by introducing chemotherapeutic moieties or tumour-specific markers to the PS for targeted anti-cancer therapy.<sup>12</sup> Introduction of functional groups, axially or peripherally to Pcs also decreases their aggregation in aqueous interfaces while alleviating their hydrophobicity.<sup>13</sup> Histone deacetylases (HDACs), regulators of reversible histone acetylation play a role in carcinogenesis, and are potential targets for anti-cancer treatments.<sup>14–16</sup> Inhibition of HDACs is shown to induce cell cycle arrest, promote cell death, modulate immune responses, and inhibit angiogenesis.<sup>17</sup> Histone deacetylase inhibitor (**HDACi**) treatments are mainly approved for haematological malignancies.<sup>18,19</sup> Examples include vorinostat, belinostat, panobinostat and romidepsin for cutaneous T-cell lymphoma, peripheral T-cell lymphoma, multiple myeloma and cutaneous T-cell lymphoma, respectively.<sup>17,18</sup> Considering the high HDAC expression observed in certain solid tumours, (such as high HDAC6 expression in breast cancer),<sup>17</sup> the success of **HDACi** treatments in haematological cancers introduced them into clinical trials for targeting solid tumours. However, the results were controversial: **HDACi** monotherapies in solid tumours remained ineffective while leading to toxic side effects,<sup>20</sup> in contrast, combinatorial

<sup>a</sup>Faculty of Medicine, Immunology Department, Yeditepe University, 34755 Ataşehir, İstanbul, Turkey. E-mail: gulderen.ydemirel@yeditepe.edu.tr

<sup>b</sup>Department of Chemistry, Gebze Technical University, 41400 Gebze, Kocaeli, Turkey. E-mail: gurek@gtu.edu.tr; datilla@gtu.edu.tr

† Electronic supplementary information (ESI) available. See DOI: 10.1039/d1ra05404j



administration of **HDACi** and chemotherapy provided beneficial results, both in animal studies and clinical trials.<sup>21–23</sup>

Being the most common malignancy among women, every year 1.5 million patients are being diagnosed with breast cancer (which accounts for 25% of all women diagnosed with cancer), and it is estimated that 12% of all women will be diagnosed with breast cancer during their lifetimes.<sup>24,25</sup> Survival rates differ between countries: the estimated 5-year survival rate is ~80% in developed countries whereas it remains below 40% in developing countries.<sup>24</sup> Due to its heterogenic nature as well as variable morphological and biological features, different clinical approaches are adopted for the treatment of the disease.<sup>26</sup> Various studies have underlined the involvement of HDAC6 and HDAC8 activities in the breast cancer, and reported that their inhibition may be a beneficial approach for treatment.<sup>27–30</sup>

Reports involving combinatorial applications of PDT and **HDACi** suggested enhanced anti-cancer activity, yet, none of them have evaluated efficacy of a **Pc** derivative as the PS agent.<sup>31–33</sup> Previously, we reported 3-hydroxypyridin-2-thione (3-HPT), a **HDACi** substituted silicon phthalocyanine derivative (**SiPc-HDACi**) exerts anti-cancer properties on breast cancer cell lines by activating programmed cell death pathways and inducing cell cycle arrest.<sup>12</sup> Herein, we synthesized and characterized either non-peripherally or peripherally 3-HPT bearing zinc (Zn) and indium (In) **Pc** derivatives, and evaluated their efficacy on breast cancer cell lines (MCF-7 and MDA-MB-231) in addition to the healthy endothelial cell line HUVEC.

## Experimental section

### Materials and methods

IR spectra were recorded between 4000 and 500  $\text{cm}^{-1}$  using a PerkinElmer Spectrum 100 FT-IR spectrometer with an attenuated total reflection (ATR) accessory featuring a zinc selenide (ZnSe) crystal. MALDI-TOF mass spectrometry analyses were carried out on Bruker micro flex LT MALDI-TOF MS spectrometer using dihydroxybenzoic acid as a matrix.  $^1\text{H}$  NMR and  $^{13}\text{C}$  NMR spectra were recorded in DMSO-d<sub>6</sub> solutions on a Varian 500 MHz spectrometer. TMS standard was used as internal standard for  $^1\text{H}$ -NMR measurements. Elemental analysis was carried out using Thermo Finnigan Flash 1112 Instrument. Singlet oxygen quantum yield ( $\Phi_{\Delta}$ ) measurements were done by Horiba Jobin-Yvon Fluorometer with Hamamatsu NIR PMT 5509 by using direct method. All solvents and chemicals were of reagent-grade quality, purchased from Sigma Aldrich Chemical Co. and Merck.

Starting compounds, 3-nitrophthalonitrile (**2a**),<sup>34</sup> 4-nitrophthalonitrile (**2b**)<sup>35</sup> and **HDACi** (1-(2-methyl-(1,1'-biphenylmethyl))-3-hydroxypyridin-2-thione)<sup>36</sup> (**1**) were synthesized according to the literature.

## Synthesis

### Phthalonitrile derivatives (**3a** and **3b**)

**3a.** A reaction flask was charged with **HDACi** (**1**) (1.78 g, 5.78 mmol), 3-nitrophthalonitrile (**2a**) (1.00 g, 5.78 mmol) and dry DMF (5 mL) at room temperature. Then, anhydrous  $\text{K}_2\text{CO}_3$

(2.50 g, 18.00 mmol) was added portionwise and the reaction mixture was stirred at room temperature under argon atmosphere for 48 h. The resulting reaction mixture was poured into water (400 mL) to give precipitates which were then filtered and further washed with water. Purification by flash column chromatography ( $\text{SiO}_2$ ,  $\text{CH}_2\text{Cl}_2$ /Acetone/EtOH (15 : 1 : 0.2)) gave the target product **3a** (597 mg, 1.72 mmol) in 89% yield as yellow solid.  $^1\text{H}$  NMR (500 MHz,  $\text{CDCl}_3$ )  $\delta$  (ppm): 7.79–7.73 (m, 1H), 7.52 (dd,  $J$  = 10.0, 6.3 Hz, 1H), 7.46–7.40 (m, 1H), 7.36 (d,  $J$  = 11.0 Hz, 4H), 7.26 (s, 1H), 7.19 (d,  $J$  = 7.0 Hz, 1H), 6.97 (dd,  $J$  = 8.9, 3.8 Hz, 1H), 6.68 (dd,  $J$  = 8.7, 5.5 Hz, 1H), 5.87 (d,  $J$  = 4.2 Hz, 2H), 2.26 (s, 2H).  $^{13}\text{C}$  NMR (125 MHz,  $\text{CDCl}_3$ )  $\delta$  (ppm): 174.6, 159.3, 153.5, 141.1–125.9, 120.1, 117.0, 115.3, 112.8, 110.8, 105.6, 58.9, 20.6. IR (ATR-thin film)  $\nu_{\text{max}}/\text{cm}^{-1}$ : 3025, 2900–2800, 2230, 1621, 1575, 1456, 1398, 1266. MALDI-TOF (*m/z*) calc. for  $\text{C}_{27}\text{H}_{19}\text{N}_3\text{OS}$ : 433.53; found: 433.34 [M]<sup>+</sup>.

**3b.** A reaction flask was charged with **HDACi** (**1**) (1.78 g, 5.78 mmol), 4-nitrophthalonitrile (**2b**) (1.00 g, 5.78 mmol) and dry DMF (5 mL) at room temperature as described for the synthesis of **3a** gave compound **3b** (650 mg, 1.87 mmol) in 94% as yellow solid. Purification by flash column chromatography ( $\text{SiO}_2$ ,  $\text{CH}_2\text{Cl}_2$ /acetone/EtOH (15 : 1 : 0.2)) gave the target product **3b** (617 mg, 1.78 mmol) in 89% as yellow solid.  $^1\text{H}$  NMR (500 MHz,  $\text{CDCl}_3$ )  $\delta$  (ppm):  $\delta$  7.80 (dd,  $J$  = 6.7, 1.8 Hz, 1H), 7.77–7.71 (m, 1H), 7.43–7.18 (m, 10H), 6.75–6.68 (m, 1H), 5.91 (s, 2H), 2.29 (s, 3H).  $^{13}\text{C}$  NMR (125 MHz,  $\text{CDCl}_3$ )  $\delta$  (ppm): 174.9, 160.1, 153.6, 141.1–126.0, 121.1, 117.5, 115.6, 115.3, 110.9, 109.2, 105.6, 59.2, 20.6. IR (ATR-thin film)  $\nu_{\text{max}}/\text{cm}^{-1}$ : 3040, 2900–2800, 2232, 1620, 1570, 1455, 1398, 1265. MALDI-TOF (*m/z*) calc. for  $\text{C}_{27}\text{H}_{19}\text{N}_3\text{OS}$ : 433.53; found: 433.33 [M]<sup>+</sup>.

### Phthalocyanine derivatives (**ZnPc-1**, **ZnPc-2**, **InPc-1** and **InPc-1**)

**ZnPc-1.** To a stirred solution of phthalonitrile derivative (**3a**) (800 mg, 1.85 mmol) in dry hexanol (2 mL), dry  $\text{Zn}(\text{OAc})_2$  (170 mg, 0.92 mmol) was added. After dissolving, 3 drops of DBU was added and reaction mixture was stirred at reflux temperature for 18 h. The solvent was removed from the resulting reaction mixture with condenser. Purification by flash column chromatography ( $\text{SiO}_2$ ,  $\text{CH}_2\text{Cl}_2$  :  $\text{C}_2\text{H}_5\text{OH}$  (30 : 1)) gave **ZnPc-1** (121 mg, 0.067 mmol) in 15% yield as green color solid.  $^1\text{H}$  NMR (500 MHz, DMSO-d<sub>6</sub>)  $\delta$  (ppm):  $\delta$  8.57 (bs, 5H, ArH), 8.09–6.94 (m, ArH, 51H), 6.32–6.10 (m,  $\text{CH}_2$ , 8H), 2.34–2.16 (m,  $\text{CH}_3$ , 12H).  $^{13}\text{C}$  NMR (125 MHz, DMSO-d<sub>6</sub>)  $\delta$  (ppm): 182.14, 159.81, 156.11, 154.81, 142.30, 149.73, 145.91, 144.83, 141.92, 139.20, 137.84, 135.11, 126.18, 122.45, 122.10, 120.05, 114.82, 106.71, 59.81, 21.12. IR (ATR-thin film)  $\nu_{\text{max}}/\text{cm}^{-1}$ : 3078, 2900, 1600, 1640, 1485, 1455, 1360, 1093, 880, 744. MALDI-TOF (*m/z*) calc. for  $\text{C}_{108}\text{H}_{76}\text{N}_{12}\text{O}_4\text{S}_4\text{Zn}$ : 1799.50, found: 1799.35 [M]<sup>+</sup>. Elemental analysis (%) calc. for  $\text{C}_{108}\text{H}_{76}\text{N}_{12}\text{O}_4\text{S}_4\text{Zn}$ : C, 72.09; H, 4.26; N, 9.34; found C, 72.20; H, 4.35; N, 9.10. UV-vis (DMSO):  $\lambda_{\text{max}}$  nm ( $\log \epsilon$ ) 335 (5.10), 638 (4.56), 706 (5.28).

**ZnPc-2.** To a stirred solution of phthalonitrile derivative (**3b**) (800 mg, 1.85 mmol) in dry hexanol (2 mL) was added dry  $\text{Zn}(\text{OAc})_2$  (170 mg, 0.92 mmol) as described for the synthesis of **ZnPc-1** gave compound **ZnPc-2** (170 mg, 0.095 mmol) in 21% yield as green color solid.  $^1\text{H}$  NMR (500 MHz, DMSO-d<sub>6</sub>)



$\delta$  (ppm):  $\delta$  9.0–8.8 (m, ArH, 7H), 9.6–6.5 (m, ArH, 49H), 5.8 (s, CH<sub>2</sub>, 8H), 2.3 (m, CH<sub>3</sub>, 12H). <sup>13</sup>C NMR (125 MHz, DMSO-d<sub>6</sub>)  $\delta$  (ppm): 174.22, 161.23, 150.80, 148.15, 142.20, 136.45, 131.10, 130.05, 128.20, 126.90, 113.92, 106.9, 58.50, 21.22. IR (ATR-thin film)  $\nu$ <sub>max</sub>/cm<sup>-1</sup>: 3022, 2925, 1643, 1607, 1532, 1483, 1427, 1395. MALDI-TOF (*m/z*) calc. for C<sub>108</sub>H<sub>76</sub>N<sub>12</sub>O<sub>4</sub>S<sub>4</sub>Zn: 1799.50, found: 1799.65 [M]<sup>+</sup>. Elemental analysis (%) calc. for C<sub>108</sub>H<sub>76</sub>N<sub>12</sub>O<sub>4</sub>S<sub>4</sub>Zn: C, 72.09; H, 4.26; N, 9.34; found C, 72.15; H, 4.30; N, 9.20. UV-vis (DMSO):  $\lambda$ <sub>max</sub> nm (log  $\epsilon$ ) 354 (5.04), 608 (4.58), 672 (5.26).

**InPc-1.** To a stirred solution of phthalonitrile derivative (**3a**) (800 mg, 1.85 mmol) in dry hexanol (2 mL), dry indium(III) chloride (203 mg, 0.92 mmol) was added. After dissolving, 3 drops of DBU was added and reaction mixture was stirred at reflux temperature for 16 h. The solvent was removed from the resulting reaction mixture with condenser. Purification by flash column chromatography (SiO<sub>2</sub>, CH<sub>2</sub>Cl<sub>2</sub> : C<sub>2</sub>H<sub>5</sub>OH (40 : 1)) gave **InPc-1** (100 mg, 0.053 mmol) in 12% yield as dark green color solid. <sup>1</sup>H NMR (500 MHz, DMSO-d<sub>6</sub>)  $\delta$  (ppm):  $\delta$  9.32–6.48 (m, ArH, 56H), 5.90 (s, CH<sub>2</sub>, 8H), 2.27–1.92 (m, CH<sub>3</sub>, 12H). <sup>13</sup>C NMR (125 MHz, DMSO-d<sub>6</sub>)  $\delta$  (ppm): 178.4, 142.90, 135.65, 131.05, 130.09, 129.80, 126.90, 112.56, 104.3, 57.2, 20.1. IR (ATR-thin film)  $\nu$ <sub>max</sub>/cm<sup>-1</sup>: 3074, 2921–2851, 1610, 1483, 1450, 1350. MALDI-TOF (*m/z*) calc. for C<sub>108</sub>H<sub>76</sub>ClInN<sub>12</sub>O<sub>4</sub>S<sub>4</sub>: 1884.38, found: 1884.54 [M]<sup>+</sup>, 1853.14 [M – 2(CH<sub>3</sub>)<sup>+</sup>]. Elemental analysis (%) calc. for C<sub>108</sub>H<sub>76</sub>ClInN<sub>12</sub>O<sub>4</sub>S<sub>4</sub>Zn: C, 68.84; H, 4.07; N, 8.92; found C, 69.10; H, 4.20; N, 8.80. UV-vis (DMSO):  $\lambda$ <sub>max</sub> nm (log  $\epsilon$ ) 356 (4.59), 650 (3.15), 722 (5.55).

**InPc-2.** To a stirred solution of phthalonitrile derivative (**3b**) (800 mg, 1.85 mmol) in dry hexanol (2 mL), addition of dry indium(III) chloride (203 mg, 0.92 mmol) as described for the synthesis of **InPc-1** gave compound **InPc-2** (110 mg, 0.052 mmol) in 13% yield as dark green color solid. <sup>1</sup>H NMR (500 MHz, DMSO-d<sub>6</sub>)  $\delta$  (ppm):  $\delta$  9.51–9.02 (m, ArH, 6H), 9.02–8.23 (m, ArH, 6H), 7.86–6.53 (m, ArH, 44H), 6.1 (s, CH<sub>2</sub>, 8H), 2.8 (s, CH<sub>3</sub>, 12H). <sup>13</sup>C NMR (125 MHz, DMSO-d<sub>6</sub>)  $\delta$  (ppm): 178.05, 141.10, 135.06, 130.08, 129.98, 127.53, 126.10, 115.08, 104.33, 56.54, 20.60. IR (ATR-thin film)  $\nu$ <sub>max</sub>/cm<sup>-1</sup>: 3059, 2921, 2851, 1595, 1565, 1529, 1465, 1431, 1122. MALDI-TOF (*m/z*) calc. for C<sub>108</sub>H<sub>76</sub>ClInN<sub>12</sub>O<sub>4</sub>S<sub>4</sub>: 1884.38, found: 1885.64 [M + H]<sup>+</sup>. Elemental analysis (%) calc. for C<sub>108</sub>H<sub>76</sub>Cl<sub>2</sub>InN<sub>12</sub>O<sub>4</sub>S<sub>4</sub>Zn: C, 68.84; H, 4.07; N, 8.92; found C, 68.95; H, 4.15; N, 8.75. UV-vis (DMSO):  $\lambda$ <sub>max</sub> nm (log  $\epsilon$ ) 352 (4.62), 645 (4.25), 695 (5.42).

## In vitro studies

### Cell culture conditions

MCF-7 and MDA-MB-231 cells were cultured in high glucose (4.5 g L<sup>-1</sup>) Dulbecco's Modified Eagle's Medium (DMEM), while HUVECs were cultured in DMEM/F12 medium; both supplemented with 10% fetal bovine serum (FBS) and antibiotic solution (100 IU penicillin and 0.1 mg streptomycin) (all purchased from Gibco, Thermo Fisher Scientific, USA). HUVECs used in this study were between 8<sup>th</sup> and 10<sup>th</sup> passages whereas MCF-7 cells were at 24<sup>th</sup> and MDA-MB-231 cells were 34<sup>th</sup> passages. For evaluating compounds' cytotoxic properties under dark and light conditions, cells were seeded as 5000 cells per well into 96-well test plates as triplicates and incubated

overnight in 5% CO<sub>2</sub> containing cell culture incubator with humid environment for attachment. All compounds were dissolved in dimethyl sulfoxide (DMSO) and diluted in culture medium in order to prepare 1, 5, 25, 50 and 100  $\mu$ M solutions. The final concentration of DMSO did not exceed 0.1%, which is considered as safe in terms of cytotoxicity. Untreated cells were used as control.

For flow cytometric analyses and western blotting, 500.000 cells were seeded into 60 mm tissue culture dishes as triplicates; for confocal microscopy, cells were seeded on Millicell® EZ Slides (Merck Millipore, USA) as 20.000 cell per well and incubated overnight for attachment. Cells were treated with respective IC<sub>50</sub> doses and were irradiated 24 hours later as indicated above. After an additional 24 hours, cells were detached with trypsin-EDTA (w/phenol red, 0.25%, Gibco, Thermo Fisher Scientific, USA); for flow cytometric analyses, cells were washed twice with DPBS containing 0.1% sodium azide as a preservative, for western blotting, protein extraction was performed, followed by measuring protein concentration with Pierce™ BCA Protein Assay Kit (Thermo Fisher Scientific, USA).

### Determining cytotoxicity under dark and light conditions

Dose interval (1–100  $\mu$ M) was determined according to a study previously published.<sup>37</sup> Compounds' cytotoxic properties under dark conditions were evaluated by measuring viability after incubating cells with compounds for 24 hours. Light toxicity was evaluated by irradiating treated cells with red light at 5 mA for 34 minutes to obtain 500 mJ optical dose<sup>37</sup> after 24 hours of incubation at dark. Viability was measured after an additional 24 hours and IC<sub>50</sub> doses for each compound were calculated. Tetrakis-(4,7,10-trioxaundecan-1-sulfanyl)phthalocyaninato zinc (**ZnPc-C**) was used as a positive control in this study, applied, irradiated and analysed in the same manner.<sup>37</sup> Alamar Blue assay was used for determining viability (Sigma Aldrich, USA) which relies on the reduction in response to metabolic activity.<sup>38</sup> Absorbances were measured at 570 nm and 600 nm with a spectrophotometer (Epoch, BioTek Instruments, USA). Viability percentages were calculated according to the equation given in equation (S1).†

### Annexin V/propidium iodide staining

Apoptosis, necrosis and viability were evaluated with annexin V/propidium iodide staining, which is considered as the gold standard for apoptosis detection.<sup>39</sup> Detached cells were washed twice and then suspended in annexin V binding buffer (Bio-Vision Inc., USA), followed by staining with annexin V-FITC reagent (1  $\mu$ L/1  $\times$  10<sup>5</sup> cells) (BioVision Inc., USA) and propidium iodide (0.25  $\mu$ g/1  $\times$  10<sup>5</sup> cells) (Thermo Fisher Scientific) by incubating cells on ice for 15 minutes. Analyses were immediately performed on Beckman Coulter CytoFLEX flow cytometry system. CytExpert software was used for evaluating data.

### DNA content analysis

DNA content analysis relies on the difference DNA amount cells have through cell division stages G<sub>0/1</sub> pre-replicative cells, S (dividing cells) and G<sub>2/M</sub> (post replicative plus mitotic cells).<sup>40</sup>



Cells with fragmented DNA can also be identified and this fraction is named as “sub-G<sub>1</sub>” population. In this study, Cell Cycle Kit (Beckman Coulter) was used. Detached cells were fixed in 70% ethanol by incubating at 4 °C for an hour. Ethanol was discarded, cells were washed with PBS for one time and stained with the reagent supplied by incubating at room temperature for 40 minutes at dark. Samples were kept at 4 °C until analysis and read with Navios EX flow cytometry system (Beckman Coulter). Analyses were performed on ModFit Software (Version 5).

### Evaluation of HDAC6 and HDAC8 expressions by western blotting

Anti-HDAC6 (cat. no. 7558, Cell Signaling Technologies, USA) and anti-HDAC8 (cat. no. 685502, BioLegend Inc., USA) primary antibodies were prepared at 1 : 1000 dilutions while anti-β actin antibody (4970, Cell Signaling Technologies, USA) was prepared at 1 : 2000 dilution in tris buffered saline-Tween 20 solution (TBS-T) with 3% Blocker™ BSA (cat. no. 37520, Thermo Fisher Scientific, USA). 30 µg denatured protein samples were separated on 10% bis-acrylamide gels by running gels at 80 V for 3.5 hours at room temperature. Wet protein transfer was performed at 300 mA for 1 h to 0.45 µm PVDF membranes (cat. no. IPVH00010, Merck Millipore, USA). Membranes were blocked by incubating with 5% skimmed milk powder in TBS-T at room temperature for one hour; respective proteins were labelled by incubating membranes with primary antibody solutions overnight at 4 °C on shaker platform, followed by probing with either HRP-conjugated anti-rabbit or anti-mouse IgG secondary antibodies (7074 and 7076, respectively, both from Cell Signaling Technologies, USA) at room temperature for 1 h. Images were acquired on Vilber Fusion Pulse imaging system (Vilber, Germany).

### Fluorescence imaging

Confocal microscopy was used to determine Pc derivatives' cellular localizations and their impact on autophagy. Cells were fixed with 2% glutaraldehyde solution at 4 °C for 15 minutes. Residual aldehydes were quenched with 0.1 M glycine solution by incubating slides for one hour at room temperature, followed by permeabilization with 0.25% Triton X-100 in PBS at room temperature for an hour. Cells were blocked with TBS containing 1% Blocker™ BSA for an hour at room temperature prior to antibody incubation. Slides were washed trice between each step. For labelling mitochondria, cells were stained with an Alexa Fluor 488 conjugated anti-mitochondria antibody (Clone 113-1, Merck Millipore, USA) at 1 : 500 dilution by incubating overnight. For imaging autophagosome formation, slides were incubated overnight with LC3A/B antibody (Cell Signaling Technologies, polyclonal USA) at 1 : 200 dilution, followed by incubating with an Alexa Fluor® 488 conjugated donkey anti-rabbit secondary antibody (Abcam, polyclonal) at 1 : 100 dilution for an hour at room temperature. Antibody solutions were prepared in TBS containing 3% Blocker™ BSA. Slides were mounted with Dianova Immuno-select Antifading Mounting Medium with DAPI and visualized via Zeiss LSM 880 Airyscan inverted confocal microscope. Photos were taken by Zeiss Zen Black software (Black edition).

### Evaluation of mitochondrial activity

Mitochondrial activity was measured by dihydrorhodamine 123 (DHR123), a non-fluorescent substance which gains its fluorescent properties under oxidizing conditions and shown to identify cells with disrupted mitochondrial respiratory chain function.<sup>41</sup> In this study, 2.5 × 10<sup>5</sup> cells were incubated with 5 µM DHR123 at room temperature for 25 minutes and immediately analysed by Beckman Coulter CytoFLEX system. Analyses were performed on CytExpert software.

### Evaluation of protein expression by flow cytometry

For analysing protein expressions, 2.5 × 10<sup>5</sup> cells were washed twice with DPBS and suspended in 100 µL DPBS containing 0.1% sodium azide. Cells were labelled with Anti-CD44 PE, anti-CXCR4 PerCP/Cy5.5 and anti-CCR7 PE/Cy7 antibodies (all purchased from BioLegend Inc., Clones BJ18, 12G5 and G043H7 respectively) by incubating at room temperature for 20 minutes under dark. Each antibody was used as 5 µL per test, according to the manufacturer's instructions. Cells were washed twice, resuspended in PBS and analysed on CytoFLEX flow cytometry system. Data analysis was performed on CytExpert software.

### Statistical analyses

GraphPad Prism Software (Version 8) was used for statistical analysis. Two-way analysis of variance (ANOVA) followed by Tukey's multiple comparison test was used for comparing treatment efficiency between cell lines, while effects of the treatment within the cell lines compared to respective controls were compared by using two-way ANOVA followed by Sidak's multiple comparison test in annexin V/PI staining, western blotting and DHR123 assay. Two-way ANOVA followed by Bonferroni's multiple comparisons test was performed to investigate the significant differences in DNA content analysis. When comparing CD44, CXCR4 and CCR7 protein levels after treatment, comparisons between treatment and control groups were done with two-way ANOVA followed by Sidak's multiple comparison test. *P* values lower than 0.05 was considered as statistically significant.

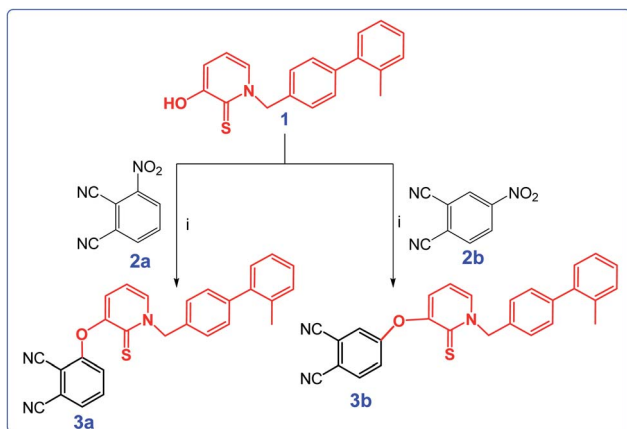
## Results and discussion

### Synthesis and characterization

The nucleophilic aromatic substitution reaction of **HDACi** (**1**) with 3-nitrophthalonitrile (**2a**) or 4-nitrophthalonitrile (**2b**) in dimethylformamide produced the intermediate phthalonitrile derivatives **3a** and **3b**, successively in high yields. The synthetic pathway and structures of **3a** and **3b** were given in Scheme 1. The structures of compound **3a** and **3b** were determined through by FT-IR, <sup>1</sup>H and <sup>13</sup>C NMR spectroscopies, ESI-MS and MALDI-TOF MS as given in Experimental section.

The <sup>1</sup>H NMR spectrum of both of the **3a** and **3b** showed the disappearance of the OH protons at around 8.6 ppm, which proved that the starting material **1** had been converted to phthalonitriles **3a** and **3b**. In addition, the IR spectra of the compounds **3a** and **3b** displayed absorptions at 2230 and 2232 cm<sup>-1</sup> respectively corresponding to the nitrile stretching frequencies.



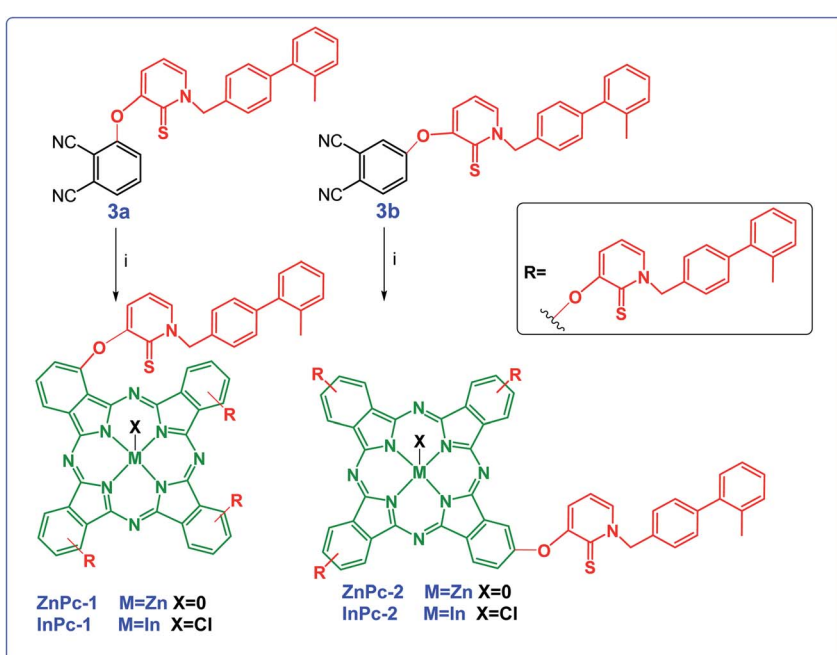


Scheme 1 Synthetic pathway of **3a** and **3b**. Reaction conditions: (i)  $\text{K}_2\text{CO}_3$ , DMF, rt, 48 h.

The cyclotetramerization reaction of the phthalonitrile derivatives to **ZnPc-1** and **ZnPc-2** was accomplished with anhydrous  $\text{Zn}(\text{OAc})_2$  in the presence of 1,8-diazabicyclo[5.4.0]undec-7-ene (DBU) and *n*-hexanol. Similarly, employing  $\text{InCl}_3$  gave the corresponding Pc derivatives, **InPc-1** and **InPc-2**. The synthetic pathway and structures of the Pc compounds (**ZnPc-1** and **ZnPc-2**, **InPc-1** and **InPc-2**) were given in Scheme 2. The newly synthesized Pc derivatives were characterized by FT-IR,  $^1\text{H}$  and  $^{13}\text{C}$  NMR, UV-vis, MALDI-TOF mass spectrometry (Fig. S1–S28†) and elemental analysis. The IR spectra clearly indicated formation of the Pc derivatives with disappearing of nitrile stretching bands at around  $2230\text{ cm}^{-1}$ . In the FT-IR spectra, aromatic C–H stretching vibrations belonging to substituted group were observed around  $3050\text{ cm}^{-1}$  while aliphatic C–H

stretching vibrations were observed between  $2900$ – $2850\text{ cm}^{-1}$  for the Pcs. The  $^1\text{H}$  NMR spectra of the Pc compounds displayed the aromatic protons resonances belonging to the **HDACi** group overlapping with Pc ring protons, while the chemical shifts of aliphatic protons of the compounds at around  $5.8$  and  $2.2\text{ ppm}$  were observed (Fig. S9, S14, S19 and S24†). A common feature of the  $^1\text{H}$  NMR spectra of all of the Pc derivatives was the broad absorptions when compared with that of the phthalonitrile derivatives, probably caused by the aggregation of the Pc which is frequently encountered at the concentrations used for NMR measurements. The signals of aromatic protons are considerably broadened and multiplied due to the formation of an isomeric mixture (Fig. S10, S15, S20 and S25†). The MALDI-TOF spectra of the Pc compounds showed molecular ion peaks supported the proposed molecular formula for these compounds (Fig. S11, S16, S21 and S26†).

Phthalocyanines are known for their unique two strong absorption Q band and Soret (B) bands, including both ultraviolet and visible regions. The electronic absorption spectra of the Pc derivatives (**ZnPc-1**, **ZnPc-2**, **InPc-1** and **InPc-2**) were studied in DMSO. In the UV-vis spectrum, Q-bands were observed at  $706$ ,  $672$ ,  $722$  and  $690\text{ nm}$  corresponding to studied Pcs (**ZnPc-1**, **ZnPc-2**, **InPc-1** and **InPc-2**) respectively (Fig. S13, S18, S23 and S28†). On the other hand, Soret bands for compounds were observed between  $350$ – $360\text{ nm}$ . The InPc derivatives (**InPc-1** and **InPc-2**) showed a shift of the Q bands to higher wavelengths in comparison with their Zn derivatives (**ZnPc-1**, **ZnPc-2**) because of central metal ion effect. When compared to substitution position of the Pcs, non-peripheral derivatives (**ZnPc-1** and **InPc-1**) displayed red shifting of Q bands as expected. All spectral data of the compounds (**3a**, **3b**, **ZnPc-1**, **ZnPc-2**, **InPc-1** and **InPc-2**) were given in ESI.†



Scheme 2 Synthetic pathway of **ZnPc1**, **InPc-1**, **ZnPc-2** and **InPc-2** and **3b**. Reaction conditions: (i) DBU, *n*-hexanol, the corresponding metal salt, 18 h.



## Photochemical properties

The singlet oxygen quantum yield ( $\Phi_{\Delta}$ ) is described as the number of molecules of singlet oxygen generated per number of photons absorbed by the sensitizer. A number of different techniques for the determination of  $\Phi_{\Delta}$  measurement of efficiency have been developed over the five decades.<sup>42-44</sup> In our work, we had applied a direct method in DMF. Singlet-oxygen phosphorescence spectra for all compounds excited with a xenon-arc source at their respective absorption maxima were recorded by a near-IR-sensitive detector. Singlet oxygen phosphorescence spectra of Pcs in DMF at equal absorbances (0.23) were obtained to directly determine  $\Phi_{\Delta}$ . Table S1† shows  $\Phi_{\Delta}$  values of all the Pcs in DMF (Fig. S29–S32†).  $\Phi_{\Delta}$  for **ZnPc-1** and **InPc-1** derivatives were obtained at same value (0.57). Although peripherally 3-HPT bearing Pcs (ZnPc-2) shown the highest value (0.73), **InPc-2** gave the lowest value (0.50) (Table S1†).

## Dark and light cytotoxicity

None of the compounds tested showed toxicity after incubation for 24 hours under dark conditions, even at high concentrations ( $p > 0.05$ ) (Fig. S33–S35†). When considering **ZnPc-HDACis**; IC<sub>50</sub> values of **ZnPc-1** on HUVECs, MCF-7 and MDA-MB-231 were reported as 72.1, 65 and 63  $\mu$ M; whereas calculated as 24.9, 16.8 and 24  $\mu$ M, respectively for **ZnPc-2** (Fig. S34†). IC<sub>50</sub> values for **InPc-HDACis** were calculated as 84.3, 67.4 and 56.5  $\mu$ M for **InPc-1**; 80.7, 56.4 and 48.4  $\mu$ M for **InPc-2** on HUVECs, MCF-7 and MDA-MB-231 cells, respectively (Fig. S35†). IC<sub>50</sub> doses for the positive control in this study, tetrakis-(4,7,10-trioxaundecan-1-sulfanyl)phthalocyaninato zinc (**ZnPc-C**) was calculated as 89.5, 63.5 and 82.4  $\mu$ M for HUVECs, MCF-7 cells and MDA-MB-231 cells, respectively (Fig. S33†).

## Evaluation of apoptosis and viability

Apoptosis is a tightly regulated cell death mechanism that is essential for the maintenance of normal cellular homeostasis by either eliminating undesired or potentially harmful cells. Dysregulations in apoptotic pathways are related to various pathological conditions including cancer.<sup>45</sup> Apoptosis is considered as the main cell death pathway in both PDT and HDAC inhibition.<sup>32</sup> Here, both **ZnPc-HDACi** derivatives decreased viability significantly for all cell lines compared to control groups while viability rates of all cell lines were significantly higher for **ZnPc-1** treated cells compared to **ZnPc-2** treatment ( $p < 0.0001$ ) (Fig. 1b). **ZnPc-1** did not induce apoptosis significantly ( $p > 0.05$ ) while **ZnPc-2** increased apoptotic cell rate in all cell lines ( $p < 0.0001$ ). Comparisons between cell lines indicated MCF-7 cells had highest late apoptotic cell population ( $p < 0.0001$ ) as well as HUVECs had significantly lower apoptosis rates compared to both MCF-7 and MDA-MB-231 cells (Fig. 1d). **ZnPc-1** treatment did not alter late apoptotic cell ratios between cell lines ( $p > 0.05$ ). However, in contrast to **ZnPc-2** which did not induce early apoptosis, **ZnPc-1** significantly increased early apoptosis in all cell lines, most significantly in MCF-7 cells which had higher early apoptotic cell rates compared to MDA-MB-231 cells ( $p < 0.05$ ) (Fig. 1c). Comparisons between treatment and control groups revealed **ZnPc-1** treatment did not alter necrotic cell population in all cell lines ( $p < 0.05$ ), however, **ZnPc-2** induced necrosis significantly on HUVECs and MCF-7 cells but not MDA-MB-231 cells ( $p < 0.0001$  and  $p < 0.01$ , respectively) (Fig. 1e). In conclusion, while both **ZnPc-HDACi** derivatives decreased viability compared to the control groups, **ZnPc-1** was reported to be less effective in terms of inducing apoptosis.

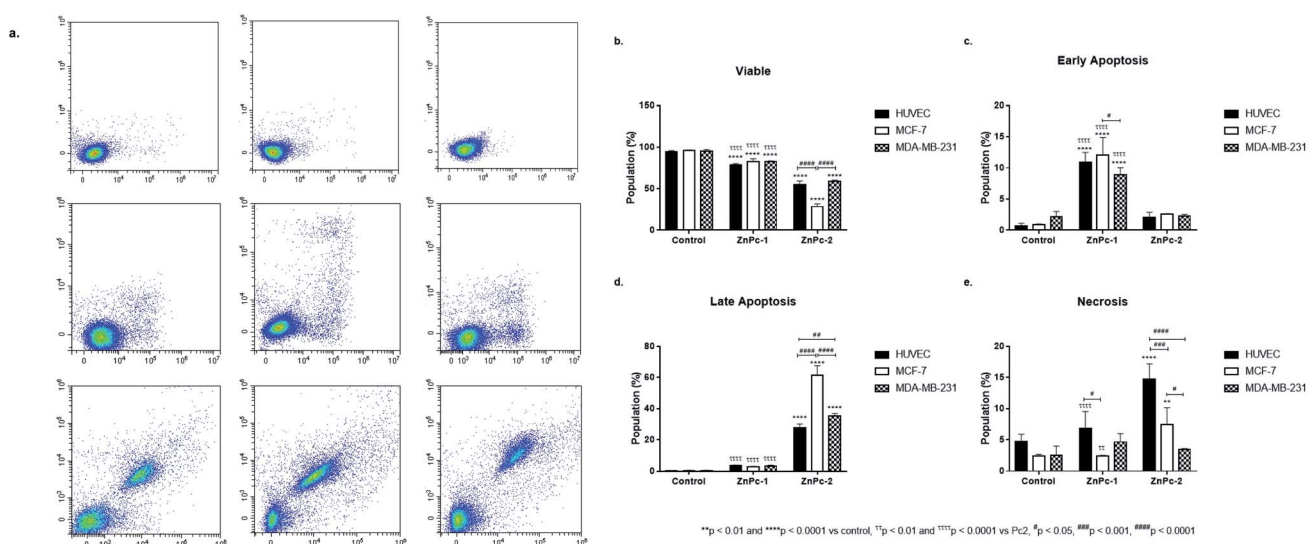


Fig. 1 Both **ZnPc-1** and **ZnPc-2** treatment decreases all cell lines' viability while promoting apoptosis. (a) Representative flow cytometry histograms. Comparisons between two different **ZnPc** derivatives in terms of (b) viability, (c) early apoptosis, (d) late apoptosis and (e) necrosis revealed that **ZnPc-1** treatment increased early apoptosis rates more effectively in all cell lines compared to **ZnPc-2**; on the other hand, late apoptotic cell populations in all cell lines were significantly higher compared to **ZnPc-1** treated counterparts, suggesting non-peripheral and peripheral substitution of HDACi residues may induce different mechanisms of action. \* denotes difference between control and treatment groups. # denotes difference between cell lines within the same treatment groups. τ indicates difference between either peripherally or non-peripherally HDACi substituted phthalocyanines bearing zinc as core metal.



When considering **InPc-HDACis**, both compounds decreased viability significantly for all cell lines compared to control groups ( $p < 0.0001$ ) while **InPc-1** treated MCF-7 cells had significantly higher viability percentage compared to their **InPc-2** treated counterparts ( $p < 0.0001$ ) (Fig. 2b). The decrease in viability rates were accompanied by an increase in both early (Fig. 2c) and late apoptosis ratios (Fig. 2d) after **InPc-1** and **InPc-2** treatments ( $p < 0.0001$ ). While no differences were observed between **InPc-1** and **InPc-2** groups in terms of early apoptosis (Fig. 2c), **InPc-1** treated HUVECs as well as MCF-7 cells had significantly lower late apoptosis rates compared to **InPc-2** treated counterparts ( $p < 0.001$  and  $p < 0.0001$ , respectively).

### DNA content analysis

DNA damage is a well-known to initiator of programmed cell death.<sup>46,47</sup> PDT applications lead to DNA damage, either targeting DNA directly or promoting ROS formation and exerting indirect effects.<sup>48</sup> Yet, the main cytotoxic product of PDT,  $^1\text{O}_2$  is thought to be not the main inducer of DNA damage due to its short lifespan and limited range unless it is generated close to DNA strands.<sup>48</sup> On the other hand, HDAC inhibition is shown to repress DNA repair proteins and increase cellular ROS, which result in DNA damage.<sup>49</sup> Former studies indicated that both Pcs and **HDACis** are shown to induce cell cycle arrest.<sup>50-59</sup> When considering the distinct natures of various PS and **HDACis**, their differential effects on cell cycle progression would be attributed to their unique mechanism of actions, and the properties of the cells investigated. In our study, **ZnPc-HDACis** did not induce cell cycle arrest on HUVECs while **ZnPc-1** led to a small but significant decrease in  $\text{G}_0/\text{G}_1$  phase ( $p < 0.05$ ) (Fig. 3b-d). In terms of cancer cell lines, **ZnPc-1** led to  $\text{G}_2/\text{M}$ -phase arrest in MCF-7 and  $\text{G}_0/\text{G}_1$ -phase arrest MDA-MB-231 ( $p < 0.0001$ ) cells,

which is accompanied by significant decrease of S phase in both cell lines ( $p < 0.0001$ ). **ZnPc-2** induced  $\text{G}_2/\text{M}$ -phase arrest in both cancer cell lines, while in contrary to **ZnPc-1**, it decreased  $\text{G}_0/\text{G}_1$  phase in MDA-MB-231 cells. This finding reveals that direct nuclear damage caused by PDT may induce  $\text{G}_2/\text{M}$  phase arrest as when considering the nuclear localization of **ZnPc-2**, and Ps targeting non-nuclear cellular compartments may tend to lead  $\text{G}_1/\text{G}_0$  or S phase arrests. In compliance with this hypothesis, both **InPc-1** and **InPc-2** increased  $\text{G}_0/\text{G}_1$  phase ( $p < 0.01$ ) in MDA-MB-231 cells and decreased  $\text{G}_2/\text{M}$  phase ( $p < 0.0001$ ) without altering S phase ( $p > 0.05$ ), indicating a  $\text{G}_0/\text{G}_1$  phase arrest (Fig. 3e-g). Similarly, both **InPc-1** and **InPc-2** derivatives increased  $\text{SubG}_1$  ( $p < 0.01$ ) and S phases ( $p < 0.0001$ ) accompanied by the decrease of  $\text{G}_2/\text{M}$  phase ( $p < 0.0001$ ) in MCF-7 cells, suggesting an S-phase arrest. When considering healthy cells, **InPc-HDACis** increased  $\text{SubG}_1$  phase ( $p < 0.01$ ) while decreasing  $\text{G}_2/\text{M}$  phase significantly in HUVECs ( $p < 0.05$  for **InPc-1** and  $p < 0.01$  for **InPc-2**, respectively) while no differences between  $\text{G}_0/\text{G}_1$  and S phases compared to control was observed ( $p > 0.05$ ). Altogether, these data suggest when considering breast cancer cells, both **ZnPc-HDACis** and **InPc-HDACis** do not lead to cell cycle arrest on healthy endothelial cells (though **InPc-HDACis** increase the hypodiploidic cell population); **ZnPc-HDACis** induce cell cycle arrest at  $\text{G}_2/\text{M}$  phase and the position of the **HDACi** moieties may alter the efficacy of the treatment while **InPc-HDACis** tend to lead accumulation in  $\text{G}_0/\text{G}_1$  or S phases according to the cell line, and the position of **HDACi** moieties do not have a major impact on cell cycle arrest.

### Evaluation of HDAC6 and HDAC8 protein levels

Both **ZnPc-1** ( $p < 0.001$ ,  $p < 0.0001$  and  $p < 0.01$  for HUVEC, MCF-7 and MDA-MB-231 cell lines, respectively) and **ZnPc-2** ( $p < 0.001$

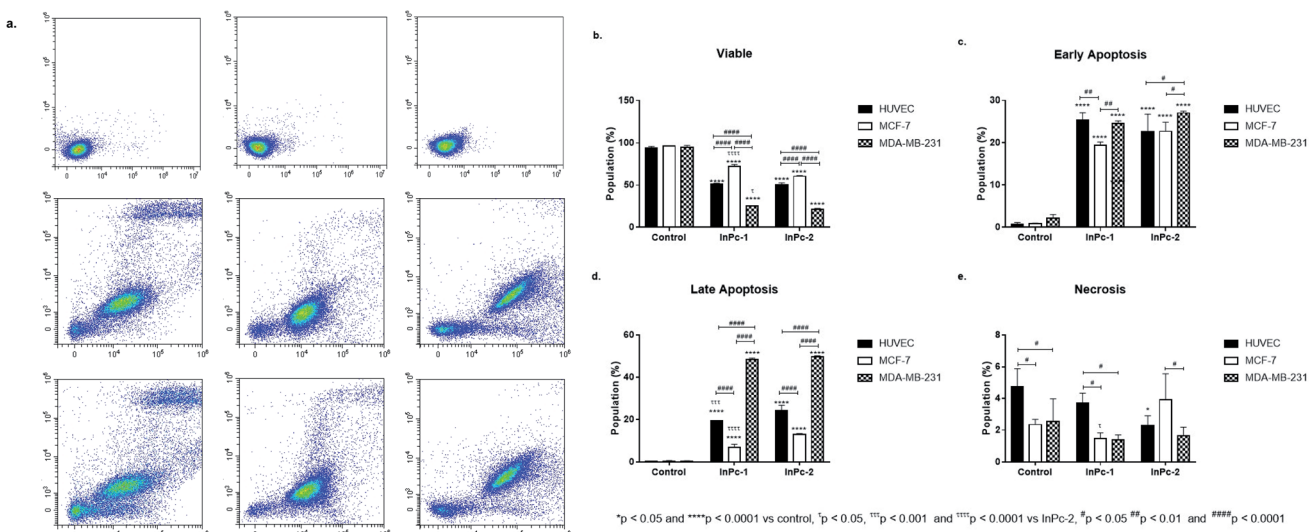
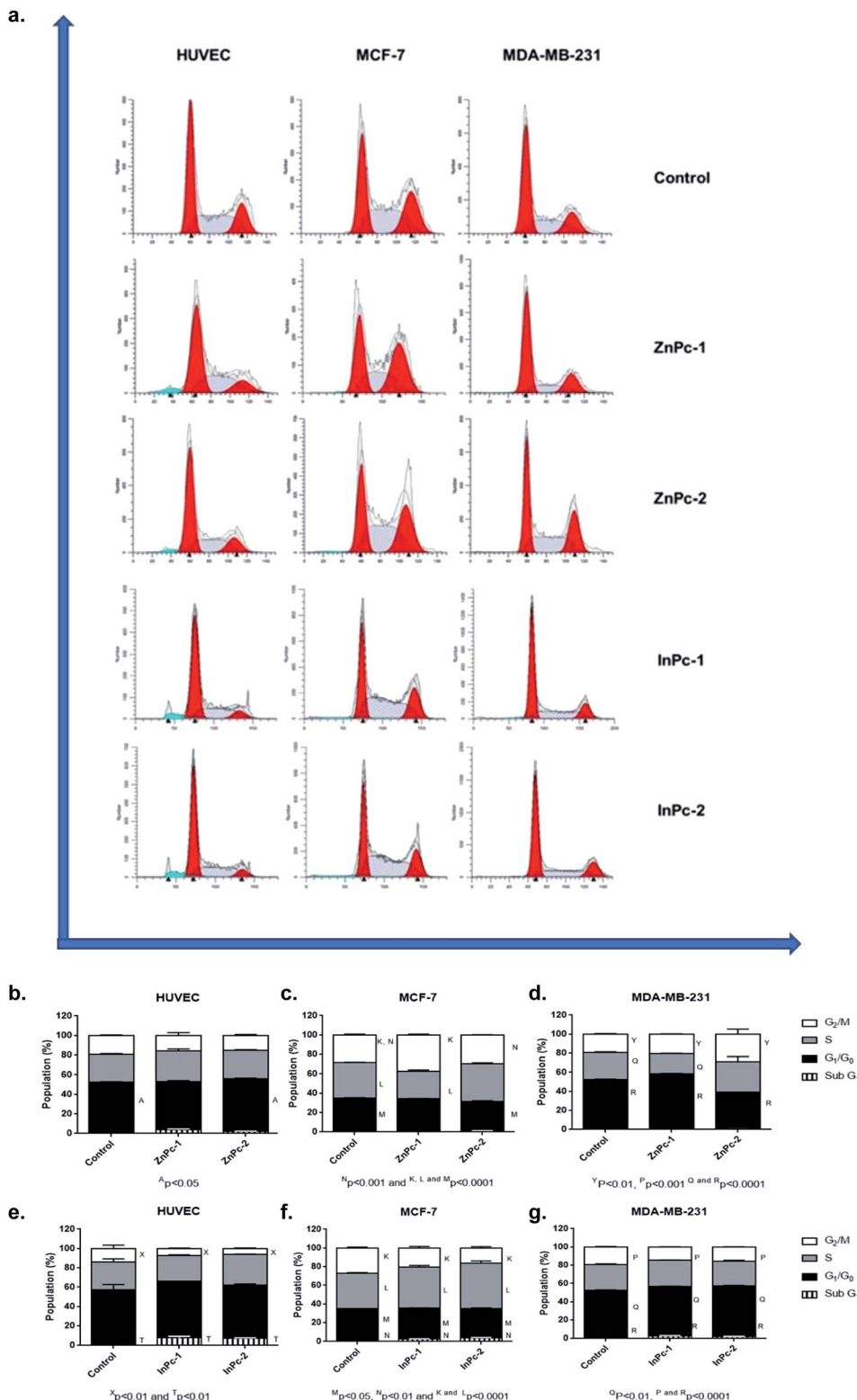
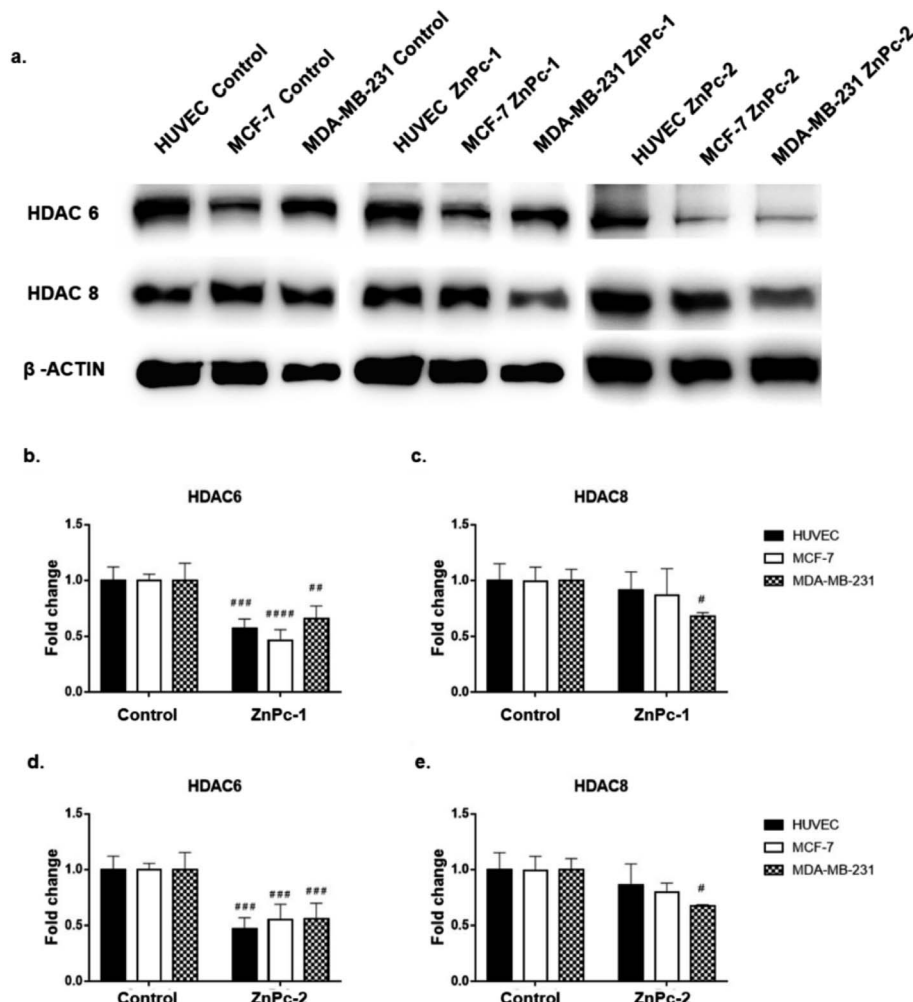


Fig. 2 Both **InPc-1** and **InPc-2** treatments decreases all cell lines' viability while promoting apoptosis. (a) Representative flow cytometry histograms. Comparisons between two different **InPc** derivatives in terms of (b) viability, (c) early apoptosis, (d) late apoptosis and (e) necrosis. **InPc-1** and **InPc-2** induces both early and late apoptosis in all cell lines. While substitution position of **HDACi** residues have no effect on early apoptosis rates, **InPc-1** treatment led significantly higher viability accompanied with lower late apoptosis rates in MCF-7 cells compared to **InPc-2** treatment. \* denotes difference between control and treatment groups, # denotes difference between cell lines within the same treatment groups and  $\tau$  indicates difference between either peripheral or non-peripheral **HDACi** substituted phthalocyanines bearing indium as core metal.





**Fig. 3** DNA content analysis upon treatment with ZnPc-HDACi and InPc-HDACi derivatives. (a) Representative histograms of DNA content. (b) Both ZnPc-1 and ZnPc-2 treatments did not lead to cell cycle arrest in HUVECs. (c) Both ZnPc-1 and ZnPc-2 increased G<sub>2</sub>/M phase in MCF-7 cells. (d) ZnPc-1 and ZnPc-2 induced G<sub>0</sub>/G<sub>1</sub> and G<sub>2</sub>/M phase arrests in MDA-MB-231 cells, respectively. (e) Both InPc-1 and InPc-2 treatments decreased G<sub>2</sub>/M phase in HUVECs while increasing SubG<sub>1</sub> phases. (f) Both InPc-1 and InPc-2 treatments decreased G<sub>2</sub>/M phase while inducing S-phase arrest in MCF-7 cells. (g) Both InPc-1 and InPc-2 treatments decreased G<sub>2</sub>/M phase while inducing G<sub>0</sub>/G<sub>1</sub> phase arrest in MDA-MB-231 cells.



**Fig. 4** Both ZnPc-1 and ZnPc-2 successfully decrease HDAC6 levels in all cell lines while HDAC8 levels were only decreased in MDA-MB-231 cells. (a) Representative blot image of ZnPc-1 and ZnPc-2 treated HUVECs, MCF-7 and MDA-MB-231 cells. (b) Quantification of HDAC6 upon ZnPc-1 treatment. (c) Quantification of HDAC8 upon ZnPc-1 treatment. (d) Quantification of HDAC6 upon ZnPc-2 treatment. (e) Quantification of HDAC8 upon ZnPc-2 treatment. Significance level was considered as  $p < 0.05$ . \* denotes significance between cell lines upon treatment whereas # denotes significance between treatment and control groups.

for all cell lines) treatments significantly decreased HDAC6 levels; both compounds also decreased HDAC8 levels on MDA-MB-231 cells ( $p < 0.05$ ), but not on MCF-7 cells or HUVECs (Fig. 4b and c).

Similar to **ZnPc-HDACis**, both **InPc-1** ( $p < 0.001$  for all cell lines) and **InPc-2** ( $p < 0.05$ ,  $p < 0.001$  and  $p < 0.01$  for HUVECs, MCF-7 and MDA-MB-231 cells, respectively) significantly decreased HDAC6 levels on all cell lines. **InPc-1** did not alter HDAC8 protein levels ( $p > 0.05$ ) in contrast to **InPc-2** which significantly decreased HDAC8 levels in both HUVECs ( $p < 0.05$ ) and MDA-MB-231 cells ( $p < 0.01$ ). When considering 3-HPT has an  $IC_{50}$ (nM) =  $306 \pm 69$  for HDAC6 and  $IC_{50}$ (nM) =  $3105 \pm 1649$  for HDAC8,<sup>36</sup> our results indicating successful HDAC6 inhibition in addition to a relatively weak effect on HDAC8 is compatible with the literature (Fig. 5).

In summary, both **ZnPc-HDACis** and **InPc-HDACis** decreased HDAC6 levels in cell lines tested, confirming the 3-HPT moieties' success on HDAC downregulation. Along with HDAC6,

**ZnPc-HDACis** were only shown to downregulate HDAC8 in MDA-MB-231 cells. The comparisons between **InPc-HDACis** revealed that **InPc-2** decreased HDAC8 levels in HUVECs and MDA-MB-231 cells, yet **InPc-1** remained ineffective. When considering non-peripheral **Pc-HDACis**; low penetration of **ZnPc-1** due to steric effect was further confirmed with the higher efficacy of **InPc-1** on downregulating HDAC8 levels in MDA-MB-231 cells. **ZnPc-2** was reported to be more effective in terms of downregulating HDAC6 levels in HUVECs, and MDA-MB-231 cells compared to **InPc-2** which may suggest a synergistic effect between PDT and HDAC inhibition when peripheral **Pc-HDACis** were compared. In contrast to assays evaluating the combinatorial anti-cancer activity of compounds, HDAC6 and HDAC8 protein levels were not expected to be influenced by PDT as a previous study, combining a PDT agent and a **HDACi** has indicated that HDAC activities are PDT-independent.<sup>33</sup> The **HDACi** moiety, 3-HPT, should interact with its respective targets to exert its' activity. Thus, membrane or mitochondrial

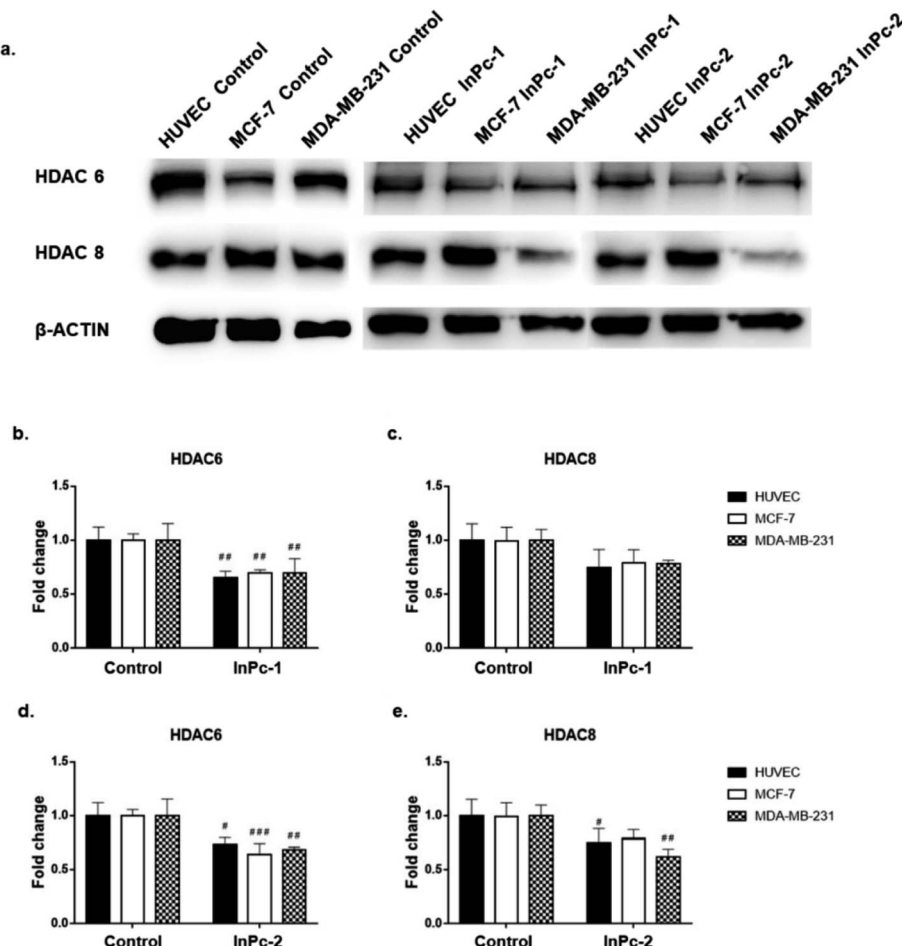


Fig. 5 Both InPc-1 and InPc-2 successfully decreased HDAC6 levels in all cell lines while HDAC8 levels were only decreased in HUVECs and MDA-MB-231 cells treated with InPc-2. (a) Representative blot images of InPc-1 and InPc-2 treated HUVECs, MCF-7 and MDA-MB-231 cells. (b) Quantification of HDAC6 upon InPc-1 treatment. (c) Quantification of HDAC8 upon InPc-1 treatment. (d) Quantification of HDAC6 upon InPc-2 treatment. (e) Quantification of HDAC8 upon InPc-2 treatment.

localization of **Pc-HDACis** may decrease their ability to inhibit HDACs. However, our HDAC evaluation strategy is limited to the semi-quantitative analysis of the protein levels and does not measure proteins' enzymatic activity. All compounds may still have disruptive effects on HDAC8 and HDAC6 proteins' deacetylating properties while preserving the proteins' integrity, which is not evaluated as a part of this study.

#### Visualization of cellular localization and autophagy

Cellular localization is an important factor that determines the anti-cancer effect of this dual system; as along with  ${}^1\text{O}_2$  generation, the **HDACi** moieties should interact with their respective targets to successfully downregulate respective proteins. For this study, the target proteins (HDAC6 and HDAC8) can be found both in nucleus and cytoplasm.<sup>60,61</sup> Confocal imaging revealed that **ZnPc-1** is either localizes to nucleoli or distributed homogeneous (which indicates cell membrane and/or cytoplasmic localization) whereas **ZnPc-2** is localized into nucleus (Fig. 6). This homogenous staining of **ZnPc-1** may explain significantly lower apoptosis rates upon treatment in contrast to

the peripheral **ZnPc-2**. As suggested by the mitochondrial staining, **ZnPc-1** disrupted mitochondrial network in HUVECs and MCF-7 cells whereas **ZnPc-2** treatment impaired mitochondrial structure in HUVECs and MDA-MB-231 cells but not MCF-7 cells. On the contrary, in addition to homogenous staining (shown in white squares), both **InPc-HDACis** are localized to the mitochondrial network (shown in pale blue squares); which is not observed in **ZnPc-1** (membrane/cytoplasmic) and **ZnPc-2** (nuclear). Neither **InPc-1** nor **InPc-2** altered mitochondrial network in HUVECs while decreasing the signal in MDA-MB-231 cells. **InPc-1** treated MCF-7 cells' mitochondrial network structure resembled control cells while **InPc-2** treatment reduced the signal, similar to MDA-MB-231 cells. On the other hand, **InPc-1** and **InPc-2** were the only compounds showing mitochondrial localization, due to the absence of a mitochondria-targeting sequence of the compounds, this overlap suggests that the **InPc-HDACis** can target mitochondria themselves.  $\text{In}^{3+}$  is known to induce mitochondrial permeability transition by disrupting proton channels located in the inner mitochondrial membrane, leading to mitochondrial oxidative stress, cytochrome c release



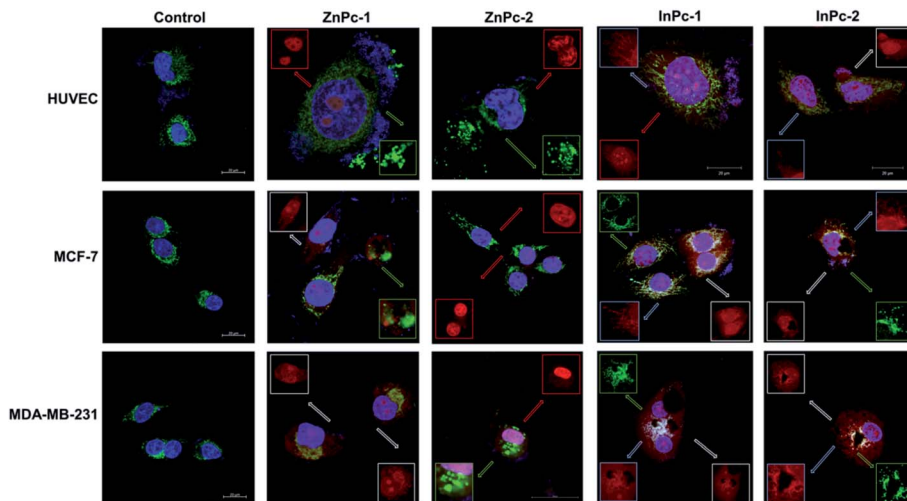


Fig. 6 Micrographs of untreated and ZnPc-1, ZnPc-2, InPc-1 and InPc-2 treated cells indicating cellular localization. Cells were stained with anti-mitochondria antibody and counterstained with DAPI. Red squares indicate deposits in nuclei and nucleoli whereas white squares indicate homogenous staining that may indicate predominant membrane/cytoplasmic localization. Disrupted mitochondria are shown in green squares. Scale bars indicate 20  $\mu$ m. All images were taken at 63X zoom with immersion oil.

and eventually apoptosis.<sup>62,63</sup> Yet, their induction of speckle formation (thus disrupting the mitochondrial network) was less prominent compared to **ZnPc-HDACis**.

Role of autophagy upon PDT is controversial as it may either lead to treatment resistance by promoting recycling damaged organelles, or initiate death signals.<sup>64</sup> Activation of apoptosis along with autophagy is reported to be crucial for an enhanced cell death response as MCF-7 cells were shown to develop PDT resistance when the autophagic response is inhibited.<sup>65,66</sup> In conclusion, it is still unclear how exactly autophagy affects the outcome of PDT.<sup>67</sup> Induction of autophagy is reported to be localization independent in PDT, and apoptosis was also observed in cells already undergoing autophagy.<sup>67</sup> We

investigated the link between localization of **Pc-HDACis** and the mode of cell death and revealed that both the core metal of the **Pc** derivative as well as the position of the **HDACi** moiety can influence the compounds' localization, and in turn, the effectiveness of the treatment. In our study, untreated cells exhibited homogenous LC3A/B staining pattern throughout the cytoplasm. **ZnPc-1** treatment induced autophagosome formation that is characterized with green puncta, indicated with yellow squares, and observed in HUVECs and MCF-7 cells but not MDA-MB-231 cells. In addition, **ZnPc-1** did not localize into autophagosomes and accumulated on either cell membrane or in nucleus which is also indicated above; suggesting **ZnPc-1** treatment may induce autophagosome formation but do not

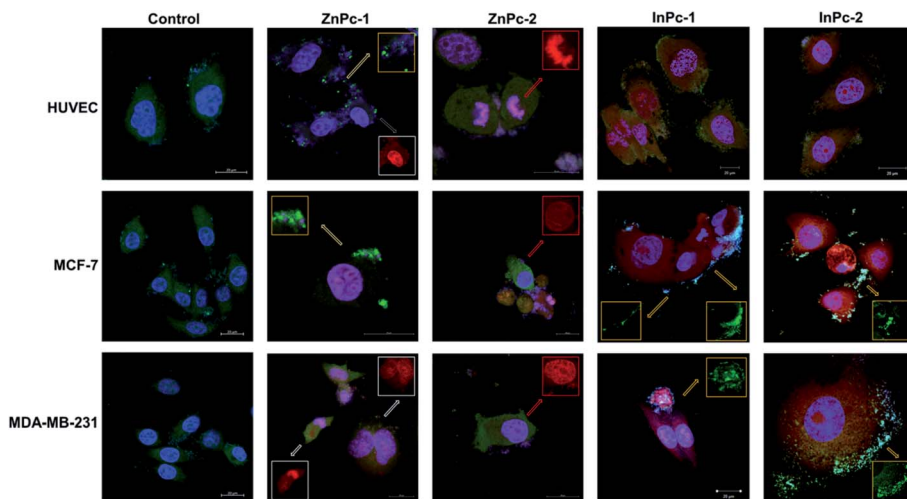
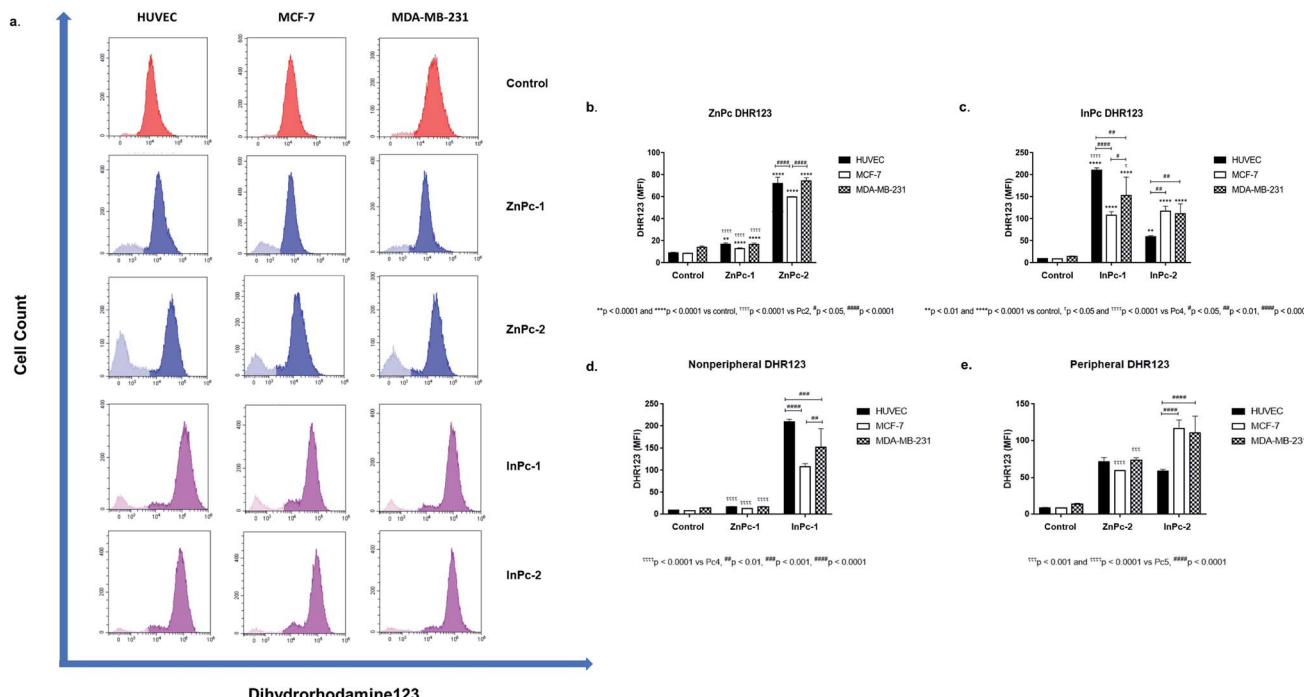


Fig. 7 Micrographs of untreated and ZnPc-1, ZnPc-2, InPc-1 and InPc-2 treated cells indicating autophagosome formation. Cells were stained with rabbit polyclonal anti-LC3A/B antibody followed by donkey anti-rabbit Alexa Fluor 488 secondary antibody and counterstained with DAPI. Puncta formations are indicated in yellow squares while red squares and white squares indicate nuclear and cytoplasmic/localization, respectively. Scale bars indicate 20  $\mu$ m. All images were taken at 63X zoom with immersion oil.





**Fig. 8** Both Zn and InPc-HDACi derivatives increased dihydrorhodamine-123 mean fluorescence intensity in all cell lines. (a) Representative flow cytometry histograms. (b) Bar graphics indicating comparisons between cell lines and DHR-123 MFI values for ZnPc-1 and ZnPc-2 treatments. (c) Bar graphics indicating comparisons between cell lines and DHR-123 MFI values for InPc-1 and InPc-2 treatments. (d) Comparisons between ZnPc-1 and InPc-1 treatments in terms of mitROS accumulation for evaluating Zn or In as core metals. (e) Comparisons between ZnPc-2 and InPc-2 treatments in terms of mitROS accumulation for evaluating Zn or In as core metals.

directly interact with autophagic lysosomes (Fig. 7). On the other hand, **ZnPc-2** treatment did not lead to autophagosome formation yet localized mainly in the nucleus as shown in Fig. 7. **InPc-1** and **InPc-2** treatment induced autophagy in both cancer cell lines, but not in HUVECs which is indicated in Fig. 7. Similar to **ZnPc-1**, neither **InPc-1** nor **InPc-2** did not localize to the autophagosomes, but the cyan colour observed in merged photos suggest that autophagosomes contain nuclear material, which is not present upon **ZnPc-1** or **ZnPc-2** treatment. Induction of autophagy upon DNA damage is suggested by various studies.<sup>68,69</sup> However, the origin of the nuclear material (genomic DNA, or mitochondrial DNA) inside the autophagosomes remains unknown.

### Evaluation of mitochondrial activity

As  ${}^1\text{O}_2$  formation depends on the availability of oxygen, mitochondria are important organelles in PDT due to their high oxygen levels.<sup>70</sup> A previous study even suggested that low levels of singlet oxygen produced in the mitochondria are two times more toxic than membrane targeting, and thrice more effective than nuclear targeting.<sup>71</sup> We evaluated mitROS accumulation by DHR123 staining. Both **ZnPc-1** ( $p < 0.001$  for HUVECs,  $p < 0.0001$  for MCF-7 and MDA-MB-231 cells) and **ZnPc-2** ( $p < 0.0001$  for all cell lines) treatments significantly increased DHR-123 MFI in all cell lines (Fig. 8b). Comparisons between **ZnPc-HDACis** indicated **ZnPc-2** treatment significantly increased DHR-123 MFI in all cell lines compared to **ZnPc-1** treatment ( $p < 0.0001$ ). A similar trend for **InPc-1** ( $p < 0.0001$  for all cell lines) and **InPc-2**

( $p < 0.001$  for HUVECs,  $p < 0.0001$  for MCF-7 and MDA-MB-231 cells) was observed when treatment and control groups were compared (Fig. 8c). Contrary to **ZnPc-HDACis**, higher DHR-123 MFI values were observed for **InPc-1** treated HUVECs as well as MCF-7 cells ( $p < 0.0001$  and  $p < 0.05$ , respectively) in comparison with peripheral **InPc-2**. Comparisons between non-peripheral Pcs indicated **InPc-1** increased DHR-123 MFI in all cell lines compared to its zinc counterpart **ZnPc-1** ( $p < 0.0001$  for all cell lines) (Fig. 8d). A similar phenomenon was observed when MCF-7 and MDA-MB-231 cells were compared after **ZnPc-2** and **InPc-2** treatments as peripheral substituted InPc derivative led to significantly increased MFI values in MCF-7 and MDA-MB-231 cells ( $p < 0.0001$  and  $p < 0.001$ , respectively), yet no difference between HUVECs was observed ( $p > 0.05$ ) (Fig. 8e).

In summary, **InPc-HDACis** which target mitochondria along with homogenous localization resulted in higher mitROS accumulation compared to **ZnPc-HDACis** (yet, **ZnPc-2** was as effective as **InPc-2** on HUVECs in terms of mitROS induction). Here, the mechanism behind the **ZnPc-HDAis**' disruptive effect on the mitochondrial network without targeting the mitochondria (observed in the confocal microscopy as green speckles), and how its' integrity is preserved after mitochondria localizing **InPc-HDACi** treatments can be questioned. This result may be an outcome of the general cellular damage induced by  ${}^1\text{O}_2$  formation as even if the PS localizes to a different site of the cell (such as **ZnPc-2** targeting nucleus), the resulting signalling cascades may alter mitochondrial network. Another possibility is the partial localization of **ZnPc-HDACis** to



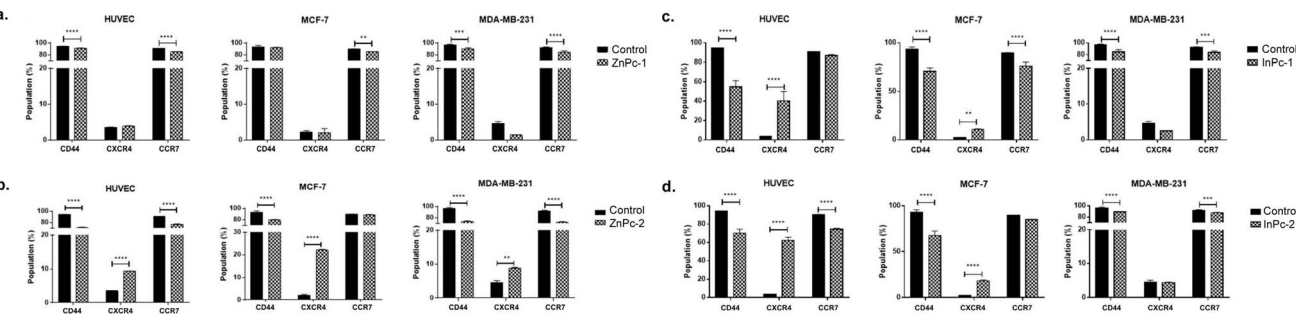


**Fig. 9** (a) ZnPc-1 decreased CCR7 protein levels in all cell lines and CD44 in HUVECs as well as MDA-MB-231 cells while increasing CXCR4 in HUVECs and MCF7 cells. (b) ZnPc-2 decreased CD44 protein levels in all cell lines while increasing CXCR4 in HUVECs and MCF7 cells. (c) InPc-1 decreased CD44 protein levels in all cell lines and CCR7 in cancer cell lines while increasing CXCR4 in HUVECs and MCF7 cells. (d) InPc-2 decreased CD44 protein levels in all cell lines and CCR7 HUVECs as well as MDA-MB-231 cells while increasing CXCR4 in HUVECs and MCF7 cells. \* denotes significance between control and treatment groups.

mitochondria-associated membranes (MAMs), the junctions where ER and mitochondria are physically connected.<sup>72</sup> Several proteins involved in cellular homeostasis reside at MAMs including the ones that take part in programmed cell death mechanisms and tumorigenesis. Yet, this hypothesis should be validated with nucleus-ER-mitochondria-compound quadruple staining along with the analysis of mitROS accumulation.

#### Evaluation of CD44, CXCR4 and CCR7 levels by flow cytometry

Leading cause of the cancer related deaths is the migration of tumour cells to form secondary lesions in distant organs. Recent studies indicate that chemokine receptor family belonging to G protein-coupled receptors play important roles in this process.<sup>73</sup> While preliminary studies suggested CXCR4 and CCR7 expression facilitates migration of tumour cells towards the chemokine gradient, today it is known that both chemokine receptors also play a role in cellular growth, endothelial adhesion and extravasation.<sup>74</sup> Upon binding to its ligand CXCL12, CXCR4 induces various signalling pathways that eventually induce gene expression, cellular motility, survival, and proliferation.<sup>75</sup> CXCR4 has been confirmed to form homo- or hetero-dimers<sup>76</sup> which activates JAK/STAT signalling pathway that promotes chemotactic responses.<sup>75</sup> Disruption of CXCL12/CXCR4 interaction significantly impairs breast cancer cells' migration towards regional lymph nodes.<sup>77</sup> Along with CXCR4, CCR7 is also shown to be highly expressed in certain malignancies including breast cancer.<sup>77</sup> CD44, a large protein family that regulates cell-ECM interactions can contribute to cancer progression including cell growth, angiogenesis, cell migration and invasion,<sup>78</sup> in addition, it also modulates CXCR4-CXCL12 signalling.<sup>79</sup>

In our study, ZnPc-1 did not alter CXCR4 protein levels in cell lines ( $p > 0.05$ ) while decreasing CD44 and CCR7 protein levels in HUVECs and MDA-MB-231 cells ( $p < 0.001$  and  $p < 0.0001$ , respectively) (Fig. 9a). ZnPc-2 led to a significant decrease in CD44 levels in all cell lines ( $p < 0.0001$ ) while increasing CXCR4 levels ( $p < 0.0001$  for HUVECs and MCF-7 cells,  $p < 0.01$  MDA-MB-231) (Fig. 9b). In addition, ZnPc-2 treatment did not alter CCR7 protein levels in MCF-7 cells while decreasing it both in HUVECs and MDA-MB-231 cells ( $p < 0.0001$ ). On the other hand, CXCR4 protein levels were increased upon ZnPc-2 treatment in

MCF-7 cells at a significantly higher rate than both HUVECs and MDA-MB-231 cells ( $p < 0.001$ , Fig. 9b). Representative flow cytometry histograms regarding ZnPc-1 and ZnPc-2 are given in Fig. S36 and S37,<sup>†</sup> respectively. InPc-1 significantly reduced CD44 protein levels in all cell lines ( $p < 0.0001$ ); similarly, CCR7 levels were decreased significantly in MCF-7 and MDA-MB-231 cells ( $p < 0.0001$  and  $p < 0.001$ , respectively) while HUVECs remain unaffected ( $p > 0.05$ ). However, InPc-1 significantly increased CXCR4 levels in HUVECs ( $p < 0.0001$ ) and MCF-7 cells ( $p < 0.01$ ), but not in MDA-MB-231 cells (Fig. 9c). InPc-1 treatment increased CXCR4 levels in HUVECs significantly compared to MCF-7 cells ( $p < 0.05$ ) while decreasing CXCR4 levels significantly in MDA-MB-231 cells, though this alteration was not significant. InPc-2 altered CD44 and CXCR4 protein levels in a similar manner with InPc-1 in HUVECs ( $p < 0.001$ ) while also decreasing CCR7 levels compared to control ( $p < 0.0001$ ) (Fig. 9d). Also, in MCF-7 cells, InPc-2 acted in a similar way with its non-peripheral counterpart by decreasing CD44 ( $p < 0.0001$ ) and increasing CXCR4 ( $p < 0.0001$ ) levels; yet, the decrease in CCR7 levels was not significant ( $p > 0.05$ ). In MDA-MB-231 cells, InPc-2 slightly but significantly decreased both CD44 and CCR7 protein levels ( $p < 0.0001$  and  $p < 0.001$ , respectively), but did not alter CXCR4 levels. Representative flow cytometry histograms regarding InPc-1 and InPc-2 are given in Fig. S38 and S39,<sup>†</sup> respectively.

In our study, all **Pc-HDACis** are shown to downregulate either CD44 or CCR7 protein levels, or both, suggesting that PDT along with HDAC inhibition may have an inhibitory effect on migration. While the effect of PDT on tumour cells' CCR7 expression is not evaluated previously, the response of immune cells to PDT in cancer, especially dendritic cells is well studied,<sup>80,81</sup> suggesting PDT promotes normal function of dendritic cells to possess anti-cancer functions compared to their untreated, tumour-educated, immunosuppressive counterparts, further underlining the importance of the presence of immune system while evaluating the efficacy of PDT in cancer treatment. However, treatment-induced alterations in CXCR4 protein levels were not in line between compounds as ZnPc-2 increased CXCR4 levels in all cell lines, especially in MCF-7 while ZnPc-1 remained ineffective in terms of CXCR4 expression. In a similar manner, InPc-1 and InPc-2 also induced CXCR4 protein expression in HUVECs and MCF-7 cells, but not MDA-MB-231 cells.



Ierano *et al.* hypothesized that **HDACi** treatment would result in decreased migration capacity due to HDACs role in cellular motility, and revealed that treatment of different cell lines (including breast, colon, lung and renal cancer) with various **HDACis** lead to CXCR4 mRNA expression along with disrupting CXCL12-mediated signalling cascades to prevent metastasis.<sup>82</sup> According to this study, increased CXCR4 levels upon **Pc-HDACi** treatment is an expected outcome and should be evaluated together with the other components of CXCL12 signalling pathway.

## Conclusions

Due to its selectivity and specificity, PDT stands out as an attractive alternative for cancer treatment.<sup>3</sup> Besides killing malignant cells by promoting ROS formation, PDT can also destroy the tumour-associated vasculature and modulate immune system to promote anti-tumoural activity.<sup>6,7</sup> Today, the majority of approved PDT protocols target superficial skin and luminal organ lesions while interstitial and intra-operative approaches are under investigation for treating solid tumours including breast tumours.<sup>83</sup>

Studies regarding combinatorial administration of **HDACi** along with PDT agents are restricted while none of them involve a **Pc** derivative for photodynamic action. Ye *et al.* synthesized four cyclometalated **Ir(III)-HDACi** complexes and investigated their anticancer efficacy on non-small cell lung cancer cell line A549 as well as its cisplatin resistant counterpart and reported that along with inhibiting HDAC activity, compounds induce mitochondrial damage and ROS production to lead apoptosis.<sup>32</sup> Evaluated on ovarian cancer cell line A2780, suberoyl-bis-hydroxamic acid (SubH)-conjugated photosensitive platinum(IV) complex showed higher toxicity than its' biologically inactive ligand substituted counterpart or cisplatin, indicating **HDACi** moieties are able to induce distinct cell death pathways than PDT or cisplatin alone.<sup>33</sup> Even in case of PDT resistance, **HDACi** pre-treatment was reported to increase the impact of PDT by promoting epigenetic alterations.<sup>31</sup> Liu *et al.* combined chlorin-6 (Ce6) and vorinostat to target hypoxia signalling pathway and reported enhanced anti-cancer activity along with decreased vascular endothelial growth factor and hypoxia inducible factor 1 alpha (HIF-1 $\alpha$ ) levels.<sup>84</sup> We have previously reported an 3-HPT substituted SiPc derivative and evaluated its' anti-cancer efficacy on MCF-7 and MDA-MB-231 cells as well as HUVECs.<sup>12</sup> According to our results, **SiPc-HDACi** had shown the greatest efficiency on the TNBC cell line MDA-MB-231 as the lowest viable cell population among with highest apoptosis rate and mitROS accumulation was observed in this cell line. In our current study, we explored biological effects of novel 3-HPT substituted Zn and In **Pc** derivatives that combines chemotherapeutic action of the **HDACi** targeting HDAC6 and HDAC8 with PDT. Comparisons between **ZnPc-HDACis** revealed that peripheral substitution of **HDACi** moieties increase cellular penetration of the **ZnPc-2** to promote a more prominent anti-cancer efficacy compared to non-peripheral **ZnPc-1**, indicating a possible steric effect for non-peripheral **HDACi** substitution. Such effect was not observed between **InPc-1** and **InPc-2**, in addition, both compounds showed a distinct localization

pattern that also targets the mitochondrial network to induce mitROS accumulation more efficiently compared to their Zn counterparts. **ZnPc-HDACis** and **InPc-HDACis** also led to cell cycle arrest in different phases of cell cycle, which may be attributed to their cellular localization. **ZnPc-2** promoted G<sub>2</sub>/M phase arrest in both cancer cell lines while **ZnPc-1**, too, led to G<sub>2</sub>/M accumulation in MCF-7 cells but not in MDA-MB-231 cells which ended up with G<sub>0</sub>/G<sub>1</sub> phase arrest. This finding suggests that direct nuclear damage caused by the PS may induce G<sub>2</sub>/M phase arrest while PS targeting non-nuclear cellular compartments may tend to lead G<sub>1</sub>/G<sub>0</sub> or S phase arrests. In compliance with this phenomenon, localizing to cytoplasm and mitochondria, **InPc-1** and **InPc-2** treatments induced accumulation in S and G<sub>0</sub>/G<sub>1</sub> phases in MCF-7 and MDA-MB-231 cells, respectively. In addition, DNA content upon treatment with both **ZnPcs** and **InPcs** did not lead to cell cycle arrest in HUVECs, which may indicate that healthy cells can cope with <sup>1</sup>O<sub>2</sub>-induced DNA damage to a greater extent in comparison with cancer cells.

It is clear that more research is required to develop new PDT agents targeting tumour cells to increase treatment efficiency. For this purpose, differences between various **Pc** derivatives' cellular impacts including their target programmed cell death pathways and localizations should be well documented to determine right PS for the photodynamic action according to the respective cancer type. Different positions for introduced **HDACis** (peripheral *vs.* non-peripheral and/or asymmetrical *vs.* symmetrical) may be evaluated to achieve optimum cellular penetration and various **HDACis** may be considered according to the targeted cancers' transcription profiles. Moreover, due to the oxygen dependent nature of PDT, *in vivo* models that can accurately reflect the outcomes of the treatment in humans to be employed for a complete evaluation of PDT drug candidates is crucial. Such evaluations would also provide insight to the compounds' effects on different cell types of the tumour, immune system, tumour vasculature, many other components play role in cancer progression, and cannot be represented *in vitro*.

## Author contributions

A. G. Gürek, G. Yanikkaya Demirel and D. Atilla contributed to the conception and design of the research. B. Aru performed all biological experiments. A. Günay and D. Atilla, synthesized and characterized **ZnPc-1**, **ZnPc-2**, **InPc-1**, **InPc-2**, and **ZnPc-C** compounds. B. Aru prepared the figures and drafted the manuscript. A. G. Gürek, G. Yanikkaya Demirel and D. Atilla edited and revised the manuscript.

## Conflicts of interest

There are no conflicts to declare.

## Acknowledgements

We thank The Scientific and Technological Research Council of Turkey (TUBITAK) for financial support (project no. 118Z693).



## References

1 J. Dang, H. He, D. Chen and L. Yin, *Biomater. Sci.*, 2017, **5**, 1500–1511.

2 P.-C. Lo, M. S. Rodríguez-Morgade, R. K. Pandey, D. K. P. Ng, T. Torres and F. Dumoulin, *Chem. Soc. Rev.*, 2020, **49**, 1041–1056.

3 X. Shi, C. Y. Zhang, J. Gao and Z. Wang, *Wiley Interdiscip. Rev.: Nanomed. Nanobiotechnol.*, 2019, **11**, e1560.

4 J. J. Schuitmaker, P. Baas, H. L. van Leengoed, F. W. van der Meulen, W. M. Star and N. van Zandwijk, *J. Photochem. Photobiol. B*, 1996, **34**, 3–12.

5 A. Juzeniene and J. Moan, *Photodiagn. Photodyn. Ther.*, 2007, **4**, 3–11.

6 P. Agostinis, K. Berg, K. A. Cengel, T. H. Foster, A. W. Girotti, S. O. Gollnick, S. M. Hahn, M. R. Hamblin, A. Juzeniene, D. Kessel, M. Korbelik, J. Moan, P. Mroz, D. Nowis, J. Piette, B. C. Wilson and J. Golab, *Ca-Cancer J. Clin.*, 2011, **61**, 250–281.

7 V. Mashayekhi, C. O. Hoog and S. Oliveira, *J. Porphyrins Phthalocyanines*, 2019, **23**, 1229–1240.

8 S. B. Brown, E. A. Brown and I. Walker, *Lancet Oncol.*, 2004, **5**, 497–508.

9 M. A. MacCormack, *Semin. Cutaneous Med. Surg.*, 2008, **27**, 52–62.

10 L. V. Zhorina, B. C. Elena, A. V. Agronskaya and G. G. Maria, presented in part at Proc. SPIE 2100, June, 1994.

11 Y. Zhang and J. F. Lovell, *Wiley Interdiscip. Rev.: Nanomed. Nanobiotechnol.*, 2017, **9**(1), e1420.

12 B. Aru, A. Günay, E. Şenkuytu, G. Yanikkaya Demirel, A. G. Gürek and D. Atilla, *ACS Omega*, 2020, **5**, 25854–25867.

13 S. Alpugan, D. Topkaya, D. Atilla, V. Ahsen, J. H. Niazi and F. Dumoulin, *J. Porphyrins Phthalocyanines*, 2017, **21**, 887–892.

14 S. Minucci and P. G. Pelicci, *Nat. Rev. Cancer*, 2006, **6**, 38–51.

15 E. Seto and M. Yoshida, *Cold Spring Harbor Perspect. Biol.*, 2014, **6**, a018713.

16 Y. Li and E. Seto, *Cold Spring Harbor Perspect. Med.*, 2016, **6**, a026831.

17 T. Eckschlager, J. Plch, M. Stiborova and J. Hrabeta, *Int. J. Mol. Sci.*, 2017, **18**, 1414.

18 J. A. Halsall and B. M. Turner, *BioEssays*, 2016, **38**, 1102–1110.

19 S. E. Bates, *N. Engl. J. Med.*, 2020, **383**, 650–663.

20 B. E. Gryder, Q. H. Sodji and A. K. Oyelere, *Future Med. Chem.*, 2012, **4**, 505–524.

21 F. M. Robertson, K. Chu, K. M. Boley, Z. Ye, H. Liu, M. C. Wright, R. Moraes, X. Zhang, T. L. Green, S. H. Barsky, C. Heise and M. Cristofanilli, *J. Exp. Ther. Oncol.*, 2013, **10**, 219–233.

22 J. Shen, C. Huang, L. Jiang, F. Gao, Z. Wang, Y. Zhang, J. Bai, H. Zhou and Q. Chen, *Biochem. Pharmacol.*, 2007, **73**, 1901–1909.

23 U. Lassen, L. R. Molife, M. Sorensen, S. A. Engelholm, L. Vidal, R. Sinha, R. T. Penson, P. Buhl-Jensen, E. Crowley, J. Tjornelund, P. Knoblauch and J. S. de Bono, *Br. J. Cancer*, 2010, **103**, 12–17.

24 M. P. Coleman, M. Quaresma, F. Berrino, J. M. Lutz, R. De Angelis, R. Capocaccia, P. Baili, B. Rachet, G. Gatta, T. Hakulinen, A. Micheli, M. Sant, H. K. Weir, J. M. Elwood, H. Tsukuma, S. Koifman, G. A. E Silva, S. Francisci, M. Santaquilani, A. Verdecchia, H. H. Storm and J. L. Young, *Lancet Oncol.*, 2008, **9**, 730–756.

25 C. E. DeSantis, J. Ma, M. M. Gaudet, L. A. Newman, K. D. Miller, A. Goding Sauer, A. Jemal and R. L. Siegel, *Cancer J. Clin.*, 2019, **69**, 438–451.

26 J. Y. S. Tsang and G. M. Tse, *Adv. Anat. Pathol.*, 2020, **27**, 27–35.

27 D. Banik, S. Noonepalle, M. Hadley, E. Palmer, M. Gracia-Hernandez, C. Zevallos-Delgado, N. Manhas, H. Simonyan, C. N. Young, A. Popratiloff, K. B. Chiappinelli, R. Fernandes, E. M. Sotomayor and A. Villagra, *Cancer Res.*, 2020, **80**, 3649–3662.

28 P. An, F. Chen, Z. Li, Y. Ling, Y. Peng, H. Zhang, J. Li, Z. Chen and H. Wang, *Oncogene*, 2020, **39**, 4956–4969.

29 V. R. Pidugu, N. S. Yarla, A. Bishayee, A. M. Kalle and A. K. Satya, *Apoptosis*, 2017, **22**, 1394–1403.

30 G. Rahmani, S. Sameri, N. Abbasi, M. Abdi and R. Najafi, *Pathol. Res. Pract.*, 2021, **220**, 153396.

31 A. Halaburková, R. Jendželovský, J. Koval, Z. Herceg, P. Fedoročko and A. Ghantous, *Clin. Epigenet.*, 2017, **9**, 62.

32 R. R. Ye, C. P. Tan, L. He, M. H. Chen, L. N. Ji and Z. W. Mao, *Chem. Commun.*, 2014, **50**, 10945–10948.

33 J. Kasparkova, H. Kostrhunova, O. Novakova, R. Kříkavová, J. Vančo, Z. Trávníček and V. Brabec, *Angew. Chem.*, 2015, **54**, 14478–14482.

34 R. D. George and A. W. Snow, *J. Heterocycl. Chem.*, 1995, **32**, 495–498.

35 J. G. Young and W. Onyebuagu, *J. Org. Chem.*, 1990, **55**, 2155–2159.

36 V. Patil, Q. H. Sodji, J. R. Kornacki, M. Mrksich and A. K. Oyelere, *J. Med. Chem.*, 2013, **56**, 3492–3506.

37 D. Atilla, N. Saydan, M. Durmuş, A. G. Gürek, T. Khan, A. Rück, H. Walt, T. Nyokong and V. Ahsen, *J. Photochem. Photobiol. A*, 2007, **186**, 298–307.

38 H. A. Byth, B. I. McNunn, I. A. Dubery and L. Bornman, *Phytochem. Anal.*, 2001, **12**, 340–346.

39 J. D. Gelles and J. E. Chipuk, *Cell Death Dis.*, 2016, **7**, e2493.

40 Z. Darzynkiewicz, *Current protocols in cytometry*, 2011, ch. 7, unit 7.2.

41 C. Sobreira, M. Davidson, M. P. King and A. F. Miranda, *J. Histochem. Cytochem.*, 1996, **44**, 571–579.

42 M. Niedre, M. S. Patterson and B. C. Wilson, *Photochem. Photobiol.*, 2002, **75**, 382–391.

43 R. Schmidt, C. Tanielian, R. Dunsbach and C. Wolff, *J. Photochem. Photobiol. A*, 1994, **79**, 11–17.

44 E. Önal, Ö. Tüncel, M. Albakour, G. G. Çelik, A. G. Gürek and S. Özçelik, *RSC Adv.*, 2021, **11**, 6188–6200.

45 S. Elmore, *Toxicol. Pathol.*, 2007, **35**, 495–516.

46 M. Redza-Dutordoir and D. A. Averill-Bates, *Biochim. Biophys. Acta, Mol. Cell Res.*, 2016, **1863**, 2977–2992.

47 A. G. Eliopoulos, S. Havaki and V. G. Gorgoulis, *Front. Genet.*, 2016, **7**, 204.



48 A. El-Hussein, M. Harith and H. Abrahamse, *Int. J. Photoenergy*, 2012, 281068.

49 J. H. Lee, M. L. Choy, L. Ngo, S. S. Foster and P. A. Marks, *Proc. Natl. Acad. Sci. U. S. A.*, 2010, **107**, 14639–14644.

50 S. L. Haywood-Small, D. I. Vernon, J. Griffiths, J. Schofield and S. B. Brown, *Biochem. Biophys. Res. Commun.*, 2006, **339**, 569–576.

51 N. Ahmad, D. K. Feyes, R. Agarwal and H. Mukhtar, *Proc. Natl. Acad. Sci. U. S. A.*, 1998, **95**, 6977–6982.

52 C. Xia, Y. Wang, W. Chen, W. Yu, B. Wang and T. Li, *Molecules*, 2011, **16**, 1389–1401.

53 J. Schmidt, W. Kuzyniak, J. Berkholz, G. Steinemann, R. Ogbodu, B. Hoffmann, G. Nouailles, A. G. Gürek, B. Nitzsche and M. Höpfner, *Int. J. Mol. Med.*, 2018, **42**, 534–546.

54 J. Shao, J. Xue, Y. Dai, H. Liu, N. Chen, L. Jia and J. Huang, *Eur. J. Cancer*, 2012, **48**, 2086–2096.

55 P. Finzer, C. Kuntzen, U. Soto, H. zur Hausen and F. Rösl, *Oncogene*, 2001, **20**, 4768–4776.

56 E. Bernhart, N. Stuendl, H. Kaltenegger, C. Windpassinger, N. Donohue, A. Leithner and B. Lohberger, *Oncotarget*, 2017, **8**, 77254–77267.

57 I. Hrgovic, M. Doll, J. Kleemann, X. F. Wang, N. Zoeller, A. Pinter, S. Kippenberger, R. Kaufmann and M. Meissner, *BMC Cancer*, 2016, **16**, 763.

58 S. Roy, K. Packman, R. Jeffrey and M. Tenniswood, *Cell Death Differ.*, 2005, **12**, 482–491.

59 Z. Dong, Y. Yang, S. Liu, J. Lu, B. Huang and Y. Zhang, *Oncotarget*, 2018, **9**, 512–523.

60 A. Chakrabarti, I. Oehme, O. Witt, G. Oliveira, W. Sippl, C. Romier, R. J. Pierce and M. Jung, *Trends Pharmacol. Sci.*, 2015, **36**, 481–492.

61 Y. Liu, L. Peng, E. Seto, S. Huang and Y. Qiu, *J. Biol. Chem.*, 2012, **287**, 29168–29174.

62 L. Yuan, J. Zhang, Y. Liu, J. Zhao, F. Jiang and Y. Liu, *J. Inorg. Biochem.*, 2017, **177**, 17–26.

63 P. K. Tsai, S. W. Wu, C. Y. Chiang, M. W. Lee, H. Y. Chen, W. Y. Chen, C. J. Chen, S. F. Yang, C. B. Yeh and Y. H. Kuan, *Ecotoxicol. Environ. Saf.*, 2020, **193**, 110348.

64 I. Mfouo-Tynga and H. Abrahamse, *Int. J. Mol. Sci.*, 2015, **16**, 10228–10241.

65 L. Y. Xue, S. M. Chiu and N. L. Oleinick, *Autophagy*, 2010, **6**, 248–255.

66 A. D. Garg, H. Maes, E. Romano and P. Agostinis, *Photochem. Photobiol. Sci.*, 2015, **14**, 1410–1424.

67 P. Mroz, A. Yaroslavsky, G. B. Kharkwal and M. R. Hamblin, *Cancers*, 2011, **3**, 2516–2539.

68 N. I. Orlotti, G. Cimino-Reale, E. Borghini, M. Pennati, C. Sissi, F. Perrone, M. Palumbo, M. G. Daidone, M. Folini and N. Zaffaroni, *Autophagy*, 2012, **8**, 1185–1196.

69 V. V. Eapen and J. E. Haber, *Autophagy*, 2013, **9**, 440–441.

70 S. M. Mahalingam, J. D. Ordaz and P. S. Low, *ACS Omega*, 2018, **3**, 6066–6074.

71 N. Rubio, S. P. Fleury and R. W. Redmond, *Photochem. Photobiol. Sci.*, 2009, **8**, 457–464.

72 S. Missiroli, S. Paternani, N. Caroccia, G. Pedriali, M. Perrone, M. Previati, M. R. Wieckowski and C. Giorgi, *Cell Death Dis.*, 2018, **9**, 329.

73 M. Kochetkova, S. Kumar and S. R. McColl, *Cell Death Differ.*, 2009, **16**, 664–673.

74 T. Kakinuma and S. T. Hwang, *J. Leukocyte Biol.*, 2006, **79**, 639–651.

75 S. Chatterjee, B. Behnam Azad and S. Nimmagadda, *Adv. Cancer Res.*, 2014, **124**, 31–82.

76 B. Ge, J. Lao, J. Li, Y. Chen, Y. Song and F. Huang, *Sci. Rep.*, 2017, **7**, 16873.

77 A. Müller, B. Homey, H. Soto, N. Ge, D. Catron, M. E. Buchanan, T. McClanahan, E. Murphy, W. Yuan, S. N. Wagner, J. L. Barrera, A. Mohar, E. Verástegui and A. Zlotnik, *Nature*, 2001, **410**, 50–56.

78 J. M. Louderbough and J. A. Schroeder, *Mol. Cancer Res.*, 2011, **9**, 1573–1586.

79 K. Fuchs, A. Hippe, A. Schmaus, B. Homey, J. P. Sleeman and V. Orian-Rousseau, *Cell Death Dis.*, 2013, **4**, e819.

80 N. Tremolec, B. Doix, C. Degavre, D. Brusa, C. Bouzin, O. Riant and O. Feron, *Cancers*, 2020, **12**(3), 545.

81 F. Zhang, Y. Zhu, G. Fan and S. Hu, *Oncol. Lett.*, 2018, **16**, 5034–5040.

82 C. Ierano, A. Basseville, K. K. To, Z. Zhan, R. W. Robey, J. Wilkerson, S. E. Bates and S. Scala, *Cancer Biol. Ther.*, 2013, **14**, 175–183.

83 A. Master, M. Livingston and A. Sen Gupta, *J. Controlled Release*, 2013, **168**, 88–102.

84 N. Liu, H. Liu, H. Chen, G. Wang, H. Teng and Y. Chang, *Colloids Surf. B*, 2020, **188**, 110753.

